FAKULTÄT FÜR
INFORMATIK

Otto-von-Guericke-University Magdeburg

Faculty of Computer Science

Institute for Intelligent Cooperating Systems

Bachelor Thesis

Comparison of Real-Time Plane Detection Algorithms on Intel RealSense

Author:

Lukas Petermann

Examiner:
Prof. Frank Ortmeier

2nd Examiner:
M.Sc. Marco Filax

Supervisor:
M.Sc. Maximilian Klockmann

December 5, 2022

Petermann, Lukas
Comparison of Real-Time Plane Detection Algorithms on Intel RealSense
Bachelor Thesis, Otto-von-Guericke-University Magdeburg, 2022.

Contents

List of Figures

1 Introduction

Man-made environments usually contain planar structures to a large extent. They are a central component in numerous use cases in the fields of Augmented and Virtual Reality, as well as robotics.

1.1 Real-Time Plane Detection

introduction

1. aktueller stand: gute und schnelle ebenenfindung wird oft gebraucht, gibt es auch schon/ist möglich
2. problem: oft sind die speziellen sensoren sehr kostenspielig
3. Daher die frage: (wie gut) ist das ganze auf bezahlbarer hardware möglich?
4. Nötig, um die Frage zu beantworten:
   - Welche Kamera(s)?
   - Welcher algorithmus?
   - Was heisst "real-time" überhaupt?
5. Problem an letzterem: nicht möglich einen einheitlich besten algorithmus auszuwählen, da ...
6. Lösung: wir wählen algorithmen aus und vergleichen diese einheitlich um die frage aus 3. zu beantworten

1.2 Intel RealSense

- Wir müssen zuerst sensoren auswählen, mit denen wir die umgebung aufnehmen
- Da, wie vorher angesprochen, der preis des sensors oft ein problem ist, wählen wir eine relativ billige (im vergleich)
- die intel sensoren sind vergleichsweise bezahlbar.
- genauer gesagt nutzen wir ...
- Zu den sensoren wird eine kostenfreie software bereit gestellt
- Über diese software lassen sich die kameras ansteuern. dazu ist in dieser software ein slam algorithmus namens rtabmap implementiert
- mit rtabmap können wir den strom aus rohdaten zu einer bestehenden karte verarbeiten, was uns ermöglicht ebenen der kompletten umgebung zu finden anstatt nur von dem aktuellen blickwinkel

2 Background

In this chapter, we present relevant literature needed to completely understand the proposed concept of chapter 3.

2.1 SLAM

SLAM (Simultaneous Localization And Mapping) algorithms aim to solve a usual problem in the field of unmanned robotics; A robot finds itself in an unknown environment and attempts to build a coherent map while keeping track of its location. The robot uses use-case-specific sensors to obtain a snapshot of its current surroundings, which it then uses to update and enhance its known map (Mapping). The robot simultaneously attempts to accurately estimate its position based on the updated map (*Localization*). The new information about its position is processed during the next map update.

Over decades of research, varieties of different (combinations of) sensors have been employed to solve this problem more accurately and efficiently. Internal odometry sensors alone can be unreliable if the robot moves over uneven or slippery surfaces. Visual sensors are, therefore, integrated into many SLAM methods, making them a Visual-SLAM (VSLAM) method. Therein, the methods can be further divided into *visual-only, visual-intertial*, and *RGB-D* SLAM [29].

Visual-only SLAM algorithms are solely based on the input of a camera. Popular VSLAM algorithms include *ORB-SLAM2* [32], $MonoSLAM$ [8], and DSO-SLAM [11].

Visual-intertial SLAM methods integrate additional sensor information from an *Inertial Measurement Unit* (IMU). The IMU provides information about the rotation, acceleration, and magnetic field around the device. These types of information generally aid the estimations based on visual input. However, the IMU data needs additional estimations, which increases the SLAM's complexity. *ORBSLAM3* [6] and *Robust Visual Inertial Odometry* (ROVIO) [4] are *visual-intertial*-based SLAM methods.

Lastly, RGB-D SLAM methods combine a monocular RGB camera and a depth sensor. This combination removes additional calculations initially needed to obtain depth information. *Dense Visual Odometry* (DVO) [22] and $RGBDSLAMv2$ [10] are instances of popular RGB-D SLAM methods.

Real-Time Appearance-Based Mapping

Real-Time Appearance-Based Mapping (RTAB-MAP) is a $VSLAM$ system with an optional IMU input, making it a *visual-intertial* SLAM. RTAB-MAP's general workflow is shown in Figure 2.1. All these inputs are combined during a synchronization step, and the results thereof are passed to RTAB-MAP's Short-Term-Memory (STM). The STM assembles a new node from the new inputs and inserts it into the map graph. Based on the newly inserted node, RTAB-MAP attempts to determine if the current location has already been visited earlier, also known as *loop closure*. If a loop closure is detected, i.e., RTAB-MAP detects the re-visiting of a known location, the map graph is optimized and thus minimized. In addition, the global map is reassembled in correspondence with the new information. The resulting map is published in the form of an *unorganized point cloud* (see Subsection 2.3.1).

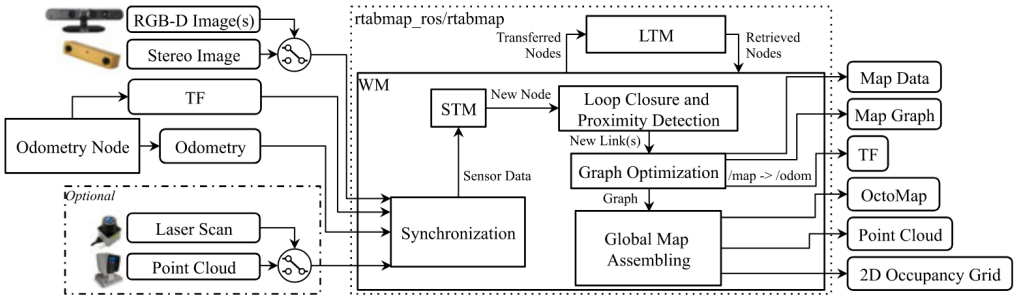

Figure 2.1: Block diagram of RTAB-MAP's system architecture. Note, that the *Point Cloud* returned by the *Global Map Assembling* is an unorganized point cloud (see Section 2.3). Taken from [24, Figure 1]

2.2 Intel Realsense

In this work, we use the Intel RealSense tracking camera T265 and the RGB-Depth(RGB-D) camera D455. A tracking camera is generally used to observe the environment and usually has a wider field of view (FOV). The primary motivation for using RGB-D cameras is depth perception. The primary differences and similarities between the T265 and the D455 are reported in Table 2.1. Beide Kameras sind stereo, die T265 hat 2 fisheye

lenses und die D455 hat 2 imagers. Dazu hat die D455 noch einen RGB sensor und einen infrarot sensor. Mit dem IR sensor und den beiden imagern wird ein tiefenbild berechnet. Durch die fisheye lenses hat die T265 mit 163° ein deutlich breiteres Sichtfeld als die D455 mit nur 111°. Die maximale FPS anzahl der D455 ergibt sich aus den individuellen FPS werten der imager sensoren und dem RGB sensor, welche beide einen maximalwert von 90 haben. Dazu sei gesagt, dass bei steigender auflösung die maximale Framerate sinkt und 90FPS nur mit einer maximalen auflösung von 640x480 möglich ist. Furthermore, both cameras have an integrated Inertial Measurement Unit (IMU) which is used to compute its position in combination with visual input.

Intel provides a software development kit, namely RealSense SDK, which allows easy and efficient use of the cameras. The SDK runs on both Windows and Ubuntu, and a ROS(Robot Operating System [1]) adaptation is also provided in Intel's Github repository [2].

	Image	Type	max. Resolution	D-FOV	Shutter	Price	max. FPS
D455	Stereo	RGB-D	1280x720	111°	global	419$	90
T265	Stereo	Tracking	848 x 800	163°	global	199$	30

Table 2.1: Intel RealSense T265 and D455 camera specifications. More information and the complete Datasheets can be found on https://www.intelrealsense.com/.

2.3 Data Formats

In the following chapters, we often refer to different data representations, namely the data that is given into a plane detection algorithm, and the exportation format of the planes. The following subsections provide necessary information and further distinctions.

2.3.1 Common Input Types

Usually, the data representation of the recorded environment falls into one of three categories:

- *unorganized* or *unstructured point cloud* (UPC)
- *organized* or *structured point cloud* (OPC)
- image:

[1] https://www.ros.org/
[2] https://github.com/IntelRealSense/realsense-ros

– Depth (DI)

– RGB (RGBI)

The input types are compared in Table 2.2. Both the organized and the unorganized point cloud store 3D coordinates. The fundamental difference between UPC and OPC is their format, In the popular point-cloud-library (PCL) data format[3], each point cloud has a *width* and a *height*. The *width* of a UPC is the number of included points, while the *height* equals 1. In contrast, the *width* and *height* of an OPC depend on the resolution of the recording camera. For instance, recording the environment with an arbitrary camera with a resolution of 640x480, each organized point cloud would have a *width* and *height* of 640 and 480, respectively. Another distinguishing factor is that the organized point cloud can only represent the environment from one angle, which leads to missing data due to sensor limitations and the occlusion of points that lie behind other points. Conversely, UPCs are neither limited to a specific viewport nor do they allow for missing points.

When considering images, a differentiation between RGB images and depth images has to be made. Depth mages are inherently similar to organized point clouds, given their resolution and two-dimensional structure. The primary difference is that the matrix stores distances to the sensor instead of 3D coordinates. RGB images are, like Depth images, stored as a 2D Matrix but instead of distances or coordinates, the matrix stores values that describe the color of a pixel. Usually, this means that each pixel stores a triple that describes a specific color by the amount of included red, green, and blue.

Input Type	Value Types	Memory Layout	0 or NaN
OPC	3D Coordinates	2D Matrix	N
UPC	3D Coordinates	1D Array	Y
DI	Distances to Sensor	2D Matrix	Y
RGBI	RGB	2D Matrix	Y

Table 2.2: Possible inputs for plane detection algorithms columns dedicated to the stored data, the memory layout, and whether the input type allows for invalid values.

It is worth noting that, in the literature, the terms "depth image", "depth map" and "organized point cloud" are used interchangeably.

lidar?

[3]http://pointclouds.org/documentation/tutorials/pcd_file_format

2.3.2 Common Output Formats

The format of the detected planes has to conform to the specific application. For instance, an architectural remodeling application would require the output to be able to contain non-rectangular shapes and holes. An algorithm that returns a set of planes represented by their convex hull would not be appropriate because it would fail to correctly represent planes like the top of a corner desk or a wall with a doorway.

Being related to the input format, the output of plane detection algorithms can be clustered as follows:

- The cartesian plane equation parameterized by its normal vector and/or its distance to the origin $(n/+d)$, *and*
- Plane inliers:
  - $3D$ inliers (3D-IN), *or*
  - $2D$ inliers (2D-IN).

A common output format is a plane parameterized by its normal vector n and its distance to the origin d. This representation describes a plane as infinitely dense and unbound, if no further information is provided, e.g. extents in certain directions.

We differentiate between the plane inliers according to the way, individual values are accessed. 3D inliers are a set of 3D coordinates that represent a plane in an unorganized point cloud. Like the point cloud itself, the inliers are accessed through their 1D index within the set. In contrast, 2D inliers are a set of indices that correspond to values in an organized point cloud, depth image, or RGB image. Moreover, some methods return a set of segmentation masks, which we also refer to as 2D inliers. Note, that we include organized point clouds in the 2D case of inliers even though the values inside are three-dimensional, as the access thereof is still grid-like.

2.4 Plane Detection

The field of plane detection has been around for decades. Most methods of detecting planar regions in unorganized point clouds are based on one of three main categories [25, 1]:

- Hough Transform (HT)
- RANSAC (RC)
- Region Growing (RG)

2.4.1 Hough Transform

The original motivation behind the Hough transform was detecting lines in images [15]. All points are sequentially processed via a voting procedure to detect the best-fitting line over a set of 2d points. Multiple lines with different orientations are fit through each given point p. Because a line in slope-intercept form parallel to the y-axis would lead to an infinite slope, the Hesse normal form is chosen as the primary line representation[9].

In Hesse normal form, an individual line can be parameterized with a pair (r, θ), with r being the orthogonal distance origin to the plane and θ being the angle between the x-axis and the line that connects the origin to the closest point on the line. This pair is also called a *Hough Space* in this context. Votes are cast on the corresponding value of θ, depending on the number of inliers within a specific *Hough Space* (r_i, θ_i). The map that connects the votes to each θ is called an *accumulator*. Finally, the best-fitting line is determined by the number of votes it received.

In the context of plane detection in 3D point clouds, a plane would be uniquely identified by the triple (ρ, θ, ϕ), with ρ being the orthogonal distance from the origin to the plane, θ being the azimuthal angle, and ϕ being the inclination. Since more parameters are needed to describe a plane in 3D, the accumulator must be adapted. Therefore, a three-dimensional accumulator is used, whereas the specific shape has been discussed [5].

2.4.2 RANSAC

RANSAC (RAndom SAmple Consensus) has been researched for decades. While many use cases revolve around image processing, it is also heavily employed in many plane detection algorithms[46, 51, 3]. RANSAC is an iterative process. Each iteration randomly samples a certain amount of data points and fits a mathematical model through them. The level of outliers determines the quality of the obtained model and preserves the best overall model.

Within the context of plane detection in 3D point clouds, an approach could involve random sampling of 3 points, fitting a plane through them, and counting the number of points within a certain range of the plane[51]. The model, in that case, could be a cartesian plane equation.

2.4.3 Region Growing

Region Growing methods are often used in the field of image or point cloud segmentation [36, 48]. RG-based segmentation methods aim to grow a set of disjoint regions from an initial selection of seed points. The regions increase in size by inserting neighboring values based on an inclusion criterion. The quality of the resulting regions depends on the choice of seed points, e.g., a very noisy seed point could decrease overall quality [30]. In the context of this work, a criterion for region growth could be the distance or curvature between a region and its adjacent data points.

2.5 Plane Detection Algorithms

The following subsections detail the necessary background knowledge of all the plane detection algorithms mentioned in this paper. Aside from the functionality of a method, we give relevant higher-level information, e.g., the expected input format and the proposed output format.

2.5.1 Robust Statistics approach for Plane Detection

Robust Statistics approach for Plane Detection (RSPD) [1] is based on region growing. After taking an unorganized point cloud as input, the procedure is divided into three phases: *Split, Grow and Merge* (see Figure 2.2).

Split The authors propose to use an octree to recursively subdivide the point cloud. The subdivision is repeated until every leaf node contains less than a threshold ε corresponding to the minimum number of points per leaf. The authors propose a value of $\varepsilon = 0.1\%$. Alternatively, the subdivision terminates if a node reaches the maximum depth level $l_O = 10$. Note, that this parameter is not referenced in [1]. However, it is used in the official implementation[4]. The subdivision is followed by a planarity test [1, Section 3.2], during which the octree is traversed bottom-up. The planarity test is comprised of three individual tests:

1. A distance test,
2. a normal divergence test, *and*
3. an inlier to outlier ratio test.

[4]https://github.com/abnerrjo/PlaneDetection

Therein, the tests are influenced by corresponding parameters. The distance test is passed, if the point-to-plane distance is smaller than the *Maximum Distance to Plane* (MDP). If the normals of a patch deviate less than the *Maximum Normal Deviation*, the second test is passed. Lastly, a patch is discarded if its percentage of outliers exceeds the *Maximum Outlier Ratio*. If all eight children of a node n are leaf nodes and fail the planarity test, n replaces its children and becomes a leaf node of its own. This procedure is repeated until the root of the octree is reached.

Grow In preparation for the growth phase, a neighborhood graph (NG) over the entire point cloud is created. Every node of NG represents one point, and an edge between two nodes exists only if a nearest-neighbor search with a neighborhood size k detects both points being in the same neighborhood. The authors use a neighborhood size of $k = 50$.

The graph construction is subsequently followed by a breadth-first-search, during which a point x is inserted into a planar patch p if it satisfies the following conditions:

- x is not included in any patch *and*
- x satisfies the inlier conditions for p:
  - The distance d of x to p is smaller than a threshold θ_d (see Eq. 2.1) *and*
  - The angle ϕ between the normals vectors of x and p is less than a threshold θ_a (see Eq. 2.2).

$$d = |(x - p.center) \cdot p.normal| < \theta_d \tag{2.1}$$

$$\phi = acos(|x.normal, p.normal|) < \theta_a \tag{2.2}$$

Merge In the last phase, the previously grown patches are merged. Two planar patches P_1 and P_2 can be merged, if the following conditions are met:

- The octree nodes of P_1 and P_2 are adjacent,
- $P_1.n$ and $P_2.n$ have a divergence within a tolerance range *and*
- at least one inlier of P_1 satisfies the inlier conditions(see Eq. 2.1+2.2) from P_2 and vice versa.

This phase returns all maximally merged planar patches, i.e. the final planes.

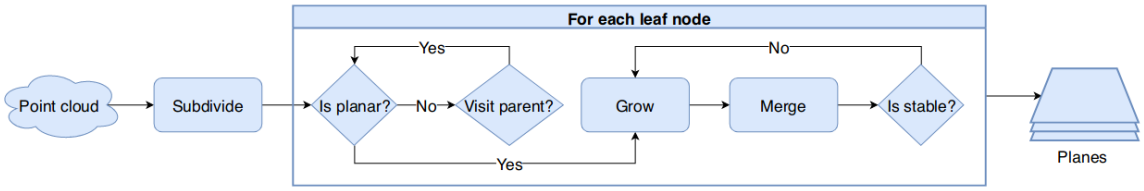

Figure 2.2: The RSPD plane detection pipeline. Taken from [1, Figure 2].

2.5.2 Oriented Point Sampling

Oriented Point Sampling (OPS) [46] accepts an unorganized point cloud as input.

First, a sample of points is uniformly selected. Sample sizes of $\alpha_s \in [0.3\%, 3\%]$ are used in the Evaluation in [46, Table 3]. The normal vectors of these points are estimated using SVD and the k nearest neighbors (KNN), which are obtained using a k-d tree. An inverse distance weight function is employed to prioritize neighboring points that are closer to the sample of which the normal vector is currently being estimated.

After normal estimation, one-point-RANSAC is performed. Usual RANSAC implementations sample three points to fit a plane. However, OPS fits a plane with only one sample point and its normal vector and counts the number of points where the distance to the plane is smaller than a *minimum-distance parameter* θ_h. Moreover, this number of inliers must exceed a *minimum plane size* threshold θ_N, for a plane to be accepted. Once a plane with the most inliers is obtained, its normal vector is re-estimated using SVD on all inliers, and all inliers are removed from the point cloud. Furthermore, the number of needed iterations I is adaptively determined in each iteration, see Equation 2.3.

$$I = \frac{\log(1-p)}{\log(1-(1-e))}, \tag{2.3}$$

where e is the ratio of outliers left in the point cloud, and p is a tuneable parameter that corresponds to the likelihood that a random sample includes no outliers. This process is repeated until the number of remaining points falls below a predefined threshold θ_N. After termination, smaller detected planes are merged if they pass a coplanarity test. After a successful merging of planes, the normal of the resulting plane is calculated via singular value decomposition (SVD).

2.5.3 3D Kernel-based Hough Transform

With the 3D Kernel-based Hough Transform (3D-KHT), Limberger and Oliveira [25] propose a hough transform-based plane detection method, that accepts unorganized point clouds as input.

The point cloud is spatially subdivided. The authors propose the usage of octrees over k-d trees because the k-d tree lacks efficiency in creation and manipulation. Furthermore, the octree succeeds in capturing the shapes inside the point cloud, while the k-d tree does not. The octree level, at which the algorithm starts to check for approximate coplanarity under nodes is adjusted through the corresponding parameter s_{level}.

Approximate coplanarity of a point cluster is evaluated based on its eigenvalues and two parameters s_α, s_β. Therein, s_α corresponds to the tolerance regarding noise, and s_β corresponds to the tolerance regarding the anisotropy of the included points. The authors report good results with $s_\alpha = 25$ and $s_\beta = 6$.

Each leaf inside the octree continues subdividing until the points inside a leaf node are considered approximately coplanar, or the number of points is smaller than a minimum-points threshold s_{ps}. The authors recommend $s_{ps} = 30$ for large point clouds. However, no definition of large in this context is given. After the approximately coplanar nodes are refined by removing outliers, a plane is fit through the remaining points.

This plane π can, in polar coordinates, be uniquely described by a triple (ρ, θ, ϕ). Inspired by Borrmann et al. [5], an accumulator ball (Fig. 2.3b) is used for the voting procedure because the cells in polar regions are smaller (and therefore contain fewer normal vectors) in three-dimensional accumulator arrays, as portrayed in Figure 2.3a. Furthermore, the discretization of the accumulator is determined by tuneable parameters, namely ϕ_{num} and ρ_{num}. No additional parameter is employed for the discretization of ρ, as this is allocated as needed during the voting procedure. The authors use $\phi_{num} = 30$ and $\rho_{num} = 300$ during their evaluation.

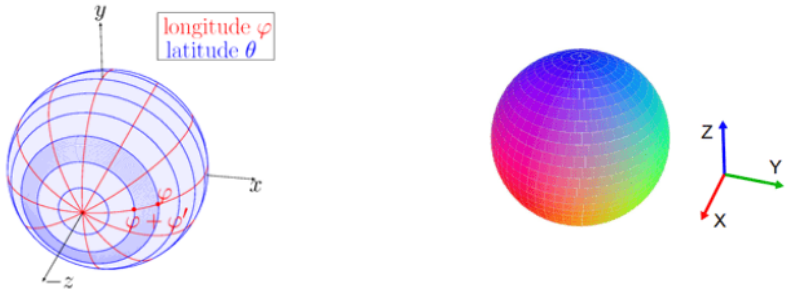

(a) (b)

Figure 2.3: Accumulator array (a), taken from [5, Figure 3]. Accumulator ball(b) used in 3D-KHT, taken from [25, Figure 5].

During the voting procedure, votes are not cast for each data point but rather on previously calculated approximately coplanar clusters. When casting a vote on a given cluster c_i with its plane (represented by (ρ, θ, ϕ)), the corresponding entry in the accumulator ball is updated. With this update, its neighboring clusters also receive a vote determined by the uncertainty value of c_i. Due to the non-discrete values of uncertainty, the votes are floating-point values as well.

All Peaks within the accumulator ball are detected in the last step. Because the votes tend to be sparsely distributed [25, Section 3.4], an auxiliary array A is used to memorize the entries inside the accumulator that are set. When an accumulator index is assigned a value for the first time, it is also added to A. Therefore, it is only necessary to iterate the auxiliary array to find peaks inside the accumulator. Furthermore, an intermediary smoothing step is performed by merging adjacent peaks inside the accumulator and storing them in A. Then, A is sorted in descending order. If a cell c in the accumulator has not yet been visited during iteration, c is considered a peak. In addition, c and its 26 neighboring cells are tagged as *visited*. That way, the most dominant plane, i.e., the one with the most votes, is detected first. Finally, the detected planes are sorted by the number of different clusters that voted for them.

2.5.4 Octree-based Region Growing

Octree-Based Region Growing (OBRG) [48] employs region growing to detect planes in UPC.

First, an unorganized point cloud is recursively subdivided using an octree. An octree node n repeatedly subdivides itself into eight children until the level of n supersedes a predefined maximum subdivision value or if the amount of contained points in n is less than a predefined minimum of included points. Saliency features are calculated for

every leaf node in preparation for the region growing step: A normal vector is obtained by performing a principle component analysis (PCA) on the points inside each leaf node. The best-fitting plane of each leaf is defined by the mean normal vector and its center point. A residual value is obtained by taking the root-mean-square (RMS) of the distance of all included points to the plane.

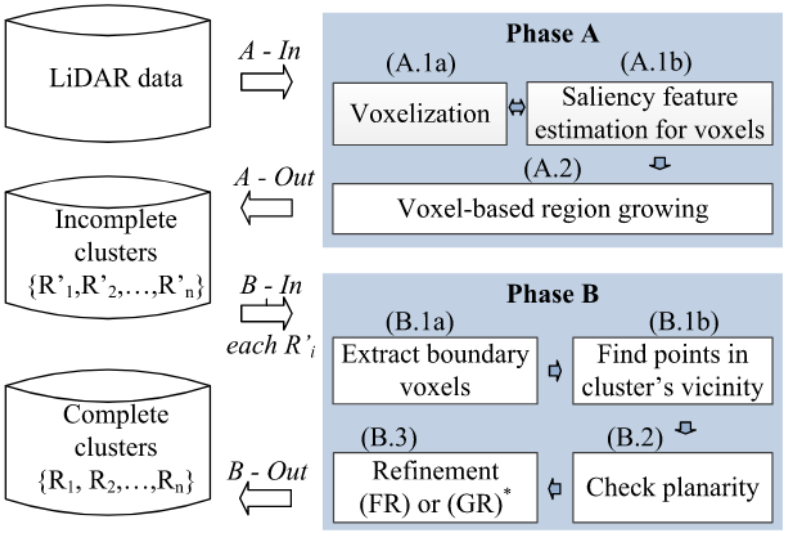

Figure 2.4: The OBRG plane detection pipeline. Taken from [48, Figure 1].

For the region growing phase, all leaf nodes are selected as individual seed points. Starting from the seed with the lowest residual value, a neighboring leaf node n is inserted into the region if n does not belong to any region and the angular divergence between both normal vectors is smaller than a predefined threshold θ_{ang}. Values between 3.5 degree and 15 degree were used during the evaluation [48, Tables 1, 4, 7]. Furthermore, if a leaf node is inserted into a region, it is also considered a starting point for a future iteration, if its residual value is lower than the corresponding threshold θ_{res}. Small values at a maximum of 0.05(m) are reported. If a region cannot be expanded, it is marked as *detected*, if its number of inliers exceeds a threshold θ_M.

Lastly, a refinement step is employed. For efficiency reasons, it is only performed on voxels at the edge of segments. Fast refinement (FR) is performed on regions that succeed in a planarity test, i.e., 70%-90% (θ_p) of included points fit the best plane [48, Section 3.4]. FR is leaf-based, and all previously unallocated neighboring nodes are added to the region if the point-to-plane distance is smaller than a distance threshold θ_d. General refinement (GR) is performed on regions that are considered non-planar. In contrast to the fast refinement, GR is point based. Therefore, points from neighboring and previously unallocated leaf nodes are considered and inserted into the region if they,

too, satisfy the inlier criterion. The refinement process returns a complete set of planar regions.

2.5.5 Probabilistic Agglomerative Hierarchical Clustering

Probabilistic Agglomerative Hierarchical Clustering (PEAC) [12] is a plane detection algorithm that takes an organized point cloud as input. The agglomerative hierarchical clustering is based on an algorithm called *line regression*[33, Section III.B]. The primary difference is that, instead of a double linked list, PEAC operates on a graph G.

First, the input organized point cloud is divided into non-overlapping nodes through the initialization of G. Each node in G has a pre-determined height H and width W, whereas H and W correspond to index ranges in the point cloud, i.e., each node contains a set of points. Then, G is refined by removing the following types of nodes and corresponding edges [12, Section III.A]:

1. Nodes that contain NaN or 0 values, e.g., missing data,
2. nodes that contain at least one point that is depth-discontinuous with its four neighbors, e.g., neighbors in the pixel space but not in coordinate space,
3. nodes with a high MSE, e.g., non-planar regions, *and*
4. nodes that share an edge with two different planes, e.g., the corners of walls.

During this step, all points inside a node share a common plane normal.

The *agglomerative hierarchical clustering* step starts with the construction of a min-MSE-heap data structure that contains the nodes of G, sorted in ascending order by the value of their MSE. The following steps are then repeated exhaustively. First, the node v that has the current minimum MSE is merged with one of its neighbors u that minimizes the merged MSE. If the merged MSE is larger than a threshold θ_{MSE}, then a plane is found and the merged node is removed from G. if MSE_{merge} is larger than a threshold θ_{MSE}, then a plane segment is found and extracted from G. Otherwise, the merged node is added back to G, joining the edges of v and u.

Lastly, a refinement step is employed. Due to the clustering of nodes that contain a set of points, certain types of artifacts can occur:

- Sawtooth,
- unused data points, *and*
- over-segmentation.

First, if not all neighbors of a node v belong to the plane of v, all points of v are added to a queue Q_{RG}. Then, region growing is performed on the points inside Q_{RG}, where the 4-connected neighbors are observed. A neighboring point n is inserted into the segment k of a point v if n does not belong to k, and the distance to k is smaller than the distance to its current segment. Additionally, n is inserted into Q_{RG}, which also happens if $n \in k$. The region growing is followed by another *agglomerative hierarchical clustering* step.

2.5.6 Fast Cylinder and Plane Extraction

Fast Cylinder and Plane Extraction (CAPE) [36] is a region growing-based algorithm that detects planes and cylinders in organized point clouds. The authors propose this algorithm as an extension of their Probabilistic Visual Odometry Framework [35].

In preparation for the region growing step, the cloud is subdivided into patches of predefined size, similar to the graph initialization of PEAC (see Section 2.5.5). A patch size of 20x20 was used in their evaluation [36, Section V.A]. Then, the planarity of the patches is tested, and a patch is considered non-planar, if:

- The amount of NaN or 0 points exceeds a threshold, *or*
- the patch has depth discontinuities,

whereas the depth discontinuities are only checked for pixels on an axis-aligned cross through the center of the patch A plane is then fit through the patch inliers by performing principle component analysis (PCA). The plane's MSE corresponds to the lowest eigenvalue, and the plane's normal vector is its eigenvector. A patch is considered planar, if its mean depth value is within the standard deviation of all depth values in the patch, plus a tolerance.

The normal vectors are converted from cartesian to spherical coordinates, thus being described by a polar angle, and an azimuth angle. These spherical normal vectors are then assorted into bins, thus building a histogram H. This histogram is now used for the region growing step. First, a set of patches C of the most frequent bin in H are obtained. Stop, if the most frequent bin yields fewer patches than a threshold k_1. The patch with the smallest MSE out of C is chosen as a seed s. In general, a 4-connected neighborhood is used in this approach, and a neighboring patch n is inserted into a region, if:

1. n is not assigned to any region,
2. the dot product of both patches normal vectors is less than a threshold T_N, *and*
3. the orthogonal distance of n's center to the region is less than $T_d(s) = l\sqrt{(1 - T_N^2)}$,

where l is the distance between the corner points of s. If a complete segment S is found, all included patches are removed from the list of remaining patches, and the bins of the histogram are updated accordingly. Lastly, if S exceeds the minimum plane size k_2, it is added to the set of detected planes.

The planarity of all segments is now assessed. This is done by calculating the covariance of all included points and, subsequently, comparing the ratio of the second largest eigenvalue to the smallest eigenvalue thereof. If this ratio exceeds a pre-determined parameter $plane_min_score$, the segment is considered a plane. Otherwise, additional steps are needed. First, the surface of a segment is checked for invariance, which is a property of open cylinders. For this task, PCA is performed on the stacked matrix of normal vectors of the segment. Then, the ratio of the first eigenvalue to the last eigenvalue of this covariance matrix, namely the condition number, is calculated. If the condition number exceeds a threshold θ_{cond}, the segment is comprised of a set of cylinders or planes [36, Section III.D].

Using the eigenvector with the smallest eigenvalue, the center points and normal vectors of all patches in the segment are then projected onto a plane. Then, multiple models are fit by performing sequential RANSAC. Planes are then fit through each model obtained by RANSAC. If the MSE of the plane is lower than the MSE of the corresponding cylinder model, the model is considered a plane, and a cylinder otherwise.

Lastly, the segments are undergone a refinement step. First, segments are eroded by removing boundary patches through the use of a 3x3 kernel. Next, the eroded segments are expanded by using a 3x3 8-neighbor kernel. The authors propose, that all patches valid for refinement are given by the difference between the expanded segment and the eroded segment. Lastly, each pixel p within the patches is added to the segment S if:

$$dist(p, S) \leq MSE_S \cdot k, \tag{2.4}$$

where k is a constant. The authors use $k = 9$ in their work.

2.5.7 Plane Extraction using Spherical Convex Hulls

As the name suggests, Plane Extraction using Spherical Convex Hulls (SCH-RG) employs spherical convex hulls to detect planes in organized point clouds. The primary concept behind this method is that the planes are not parameterized, but rather represented as a set of geometric constraints in the spherical coordinate system.

First, a set of pre-processing steps is employed. First, a bilateral filter is used for the reduction of noise. Subsequently, a normal map of the entire image is generated. To prepare for the region growing step, appropriate seeds are selected. This is effectively

done by subdividing the image into a grid, discarding non-planar cells, and choosing the cell centroids as seeds. The planarity of a cell is determined by its mean-square-error (MSE), which is calculated through all included points and the best fitting plane. This MSE is then compared against a MSE threshold.

Having obtained a set of seed points, the region growing step is employed. Each time a new seed is retrieved, all normals of the corresponding cell are gathered and transformed into the spherical domain. A queue is used for the retrieval of seeds and neighboring points. Starting from a seed s, neighboring points and their normals are sequentially retrieved. If a neighbor n is already assigned to some region or the depth difference is larger than a threshold T, it is discarded. If n is located inside of the spherical convex hull of the region of s, it is added to the region, and its neighbors are inserted into the queue. If n is not inside a convex hull, it is necessary to check whether n is outside of the so-called *cluster-permissible region* (CPR):

$$CPR(p) = \{q \in \mathbb{S} | \angle(p, q) \leq 2\theta\}, \tag{2.5}$$

where θ is an angular threshold. Note that the CPR of multiple points, e.g., a region, is determined by the intersection of all individual points. If n is outside the CPR of the current region, it is discarded. Otherwise, the convex hull is updated with n, n is added into the set of points included in the region, and its neighbors are inserted into the queue. It is worth noting, that seed points that are associated with already detected planes are discarded upon retrieval.

Lastly, dilation is performed to eliminate holes in planes. This is not further detailed in [31, Section III.B].

2.5.8 Depth Kernel-based Hough Transform

Depth Kernel-based Hough Transform (D-KHT) [47] is a Hough transform-based plane detection algorithm that accepts depth images as input.

The algorithm is performed in three stages: *Clustering, Voting,* and *Peak Detection.*

Clustering In the clustering step, a quadtree is constructed to spatially subdivide the image. A node recursively subdivides itself, until a minimum of included points s_{ms} is reached, or until the set of points is considered approximately coplanar. The latter is determined through a principle component analysis (PCA). Therein, the mean and a covariance matrix are computed. Pre-computing and subsequently referencing Summed-Area-Tables (SATs) is done to increase the efficiency of this step, leading to a constant-time calculation of the covariance matrix. If a non-planar node has less than s_{ms} points, these points are then considered non-relevant and ignored during the voting step.

Voting The clustering step returns a set of approximately coplanar point clusters. The best-fitting plane of each cluster is calculated. It is determined by the cluster's mean point, and a normal vector which is the eigenvector associated with the least eigenvalue of the covariance matrix. Two things are necessary to perform the voting step:

- An Accumulator to store the votes, *and*
- a set of gaussian kernels corresponding to the coplanar clusters.

Given the mean point $\mu_{(x,y,z)}$ and the unit normal vector $\overrightarrow{n} = (n_x, n_y, n_z)^T$ of a cluster, the center of the gaussian kernel is calculated:

$$\mu_{(\rho,\phi,\theta)} = \begin{pmatrix} \mu_x \\ \mu_y \\ \mu_z \end{pmatrix} = \begin{pmatrix} n_x\mu_x + n_y\mu_y + n_z\mu_z \\ \cos^{-1}(n_z) \\ \tan^{-1}(\frac{n_y}{n_x}) \end{pmatrix} \tag{2.6}$$

The covariance matrix of the gaussian kernel can then be calculated through first-order error propagation:

$$\Sigma_{(\rho,\phi,\theta)} = J\Sigma_{(x,y,z)}J^T, \tag{2.7}$$

where J is the Jacobi-Matrix of Equation 2.6.

An unbiased spherical accumulator, like in [5], is used to store votes. The axes of the accumulator range are in the following ranges:

$$\theta \in [-\pi, +\pi], \phi \in [0, \pi], \rho \in [0, \rho_{high}]$$

, where ρ_{high} is determined by the farthest distance between the camera and a point of the input image. The discretization of θ and ϕ are pre-determined by the user and should be based on the expected granularity of detected planes. Most likely, this also relates to the expected amount of noise. During the voting itself, the accumulator bins are incremented if they are within two standard deviations of the kernel mean $\mu_{(\rho,\phi,\theta)}$.

Peak Detection The voting step fills the bins of the accumulator with votes. A smoothing of the bins is performed to avoid oversegmentation or the detection of multiple equivalent planes. Vera et al. [47, Section 3.5] compute a convolution of the accumulator, as well as a 6-connected filter with a central weight of 0.2002 and neighbor weights of 0.1333. A hill-climbing strategy is then adopted to detect peaks in the accumulator. Each peak represents the parameterization of a detected plane. These planes are then sorted by relevance, whereas the relevance of a plane is determined by a weighted sum of the clusters that voted for the corresponding peak. The weights therein depend

more on the number of corresponding pixels of a cluster, rather than the number of samples.

All planes, parameterized by (ρ, ϕ, θ), are then transformed back into cartesian coordinates. Moreover, they are parameterized by a center point, which is defined by ρ, and a normal vector $\overrightarrow{n}$:

$$\overrightarrow{n} = \begin{pmatrix} n_x \\ n_y \\ n_z \end{pmatrix} = \begin{pmatrix} \sin\phi\cos\theta \\ \sin\phi\sin\theta \\ \cos\phi \end{pmatrix} \tag{2.8}$$

2.5.9 Depth Dependent Flood Fill

Depth Dependent Flood Fill (DDFF) [38] is a region growing-based algorithm that detects planes in organized point clouds. The algorithm builds upon and improves their previous method [39].

The algorithm starts by selecting appropriate seeds. First, the organized point cloud gets subdivided into cubes of a pre-determined size σ_{seed}. Within these cubes, the points are checked for depth discontinuities, as well as curvature discontinuities. They are evaluated against σ_{seed} and a normal orientation difference threshold θ_{ang}, respectively. If neither of the thresholds are exceeded, the center of the cube is marked as a seed for region growing.

The region growing is performed on point-level. Starting from a given seed s, a region is expanded by checking neighbors within a horizontal span. Given a horizontal span of length n, its middle pixel p, the minimum plane size σ is calculated as follows:

$$\sigma = \rho(p) = \kappa_\rho \cdot \delta(p)^2 + \gamma_\rho, \tag{2.9}$$

where $\delta(p)$ is the depth value of p, and κ_ρ, γ_ρ are tuneable parameters. If the span is growing towards the right, the pixel n that is σ pixel away from the right border is checked for membership. Additionally, n's upper and lower neighbors are also checked for membership. If n and at least one of n's vertical neighbors pass the following membership test, n and all pixels in between are added to the span of s.

1. The perpendicular distance of n to the plane defined by s and its normal is smaller than a threshold τ_{flood},
2. the euclidian distance between p and a neighboring pixel is smaller than a threshold τ_{point}, *and*

3. n is neither NaN, nor 0.

This region growing process yields a set of oversegmented planes. In a refinement step, the set of planes is reduced by performing merging of planes. First, a neighborhood graph of the rough segments is constructed. Any segments that share a border, i.e., the bordering pixels have a small euclidian distance, are connected through a bidirectional edge. The graph is traversed in a breadth-first manner, merging two connected nodes, a, b, if they satisfy the following condition:

1. the seed normals of a and b diverge less than a threshold τ_{angle}, *and*
2. the perpendicular distance between the segments is less than threshold τ_{merge}.

If a fails the membership test with its neighbor b, the membership test is repeated between b and all planes a has merged with. If this fails, the unidirectional edge (ab) is removed from the graph. Note, that the edge (ba) will be validated later, as b is subject to change through merges with other neighbors.

After a successful merge, a new centroid and normal are obtained by adding both plane normals and centroids together, while the respective amount of inliers acts as a weight.

The BFS iteration is repeated, until no merge occurs during an iteration. The authors state that, typically, no more than five iterations are needed [38, Section III.E].

The flooding under the constraint of minimum plane size leaves gaps. Therefore, as a refinement step, a two-pass algorithm is used to fill these gaps. The first pass scans top-to-bottom, and the second bottom-to-top. In both passes, horizontal strips of non-assigned pixels are detected. If the vertical neighbors have the same plane label, we mark all unmarked pixels with the same label.

2.5.10 PlaneNet

PlaneNet [28] is a deep learning-based approach to piece-wise planar reconstruction of a scene from a single RBB-Image.

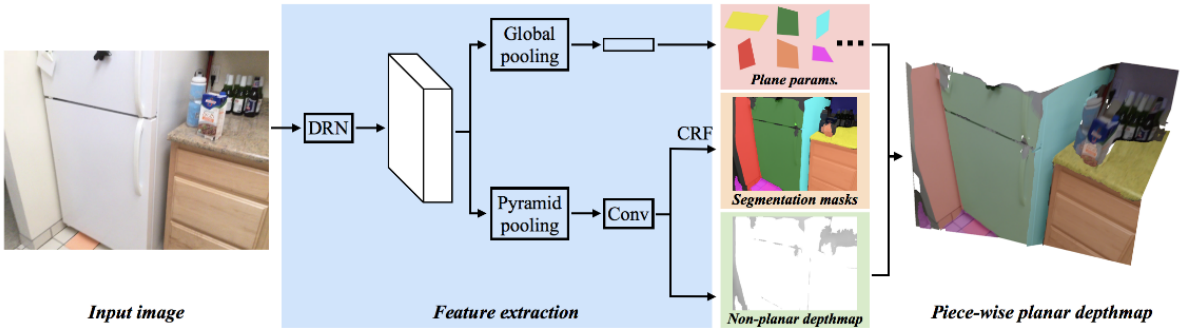

Figure 2.5: The PlaneNet Architecture. Taken from the respective paper [28, Figure 2].

The method implements a *Dilated Residual Networks* (DRNs) [52] as a precursor for a total of three output branches. These three branches predict

1. A set of plane parameters,
2. a set of corresponding segmentation masks, *and*
3. a non-planar depthmap,

as portrayed in Figure 2.5. The DRN is followed by a global pooling, or a pyramid pooling step, depending on the prediction branch. To obtain a set of plane parameters, the global pooling is followed by a fully connected layer, which produces K parameter triples. K corresponds to the number of expected planes within a scene. Liu et al. [28] use $K = 10$ during their experiments. A convolution layer is placed after the pyramid pooling the output of which is returned by the *non-planar depthmap* branch. An additional dense conditional random field (DCRF) is applied to obtain the segmentation masks.

2.5.11 PlaneRecNet

PlaneRecNet [50] is a deep learning-based approach for piece-wise plane detection and reconstruction that takes RGB images as input.

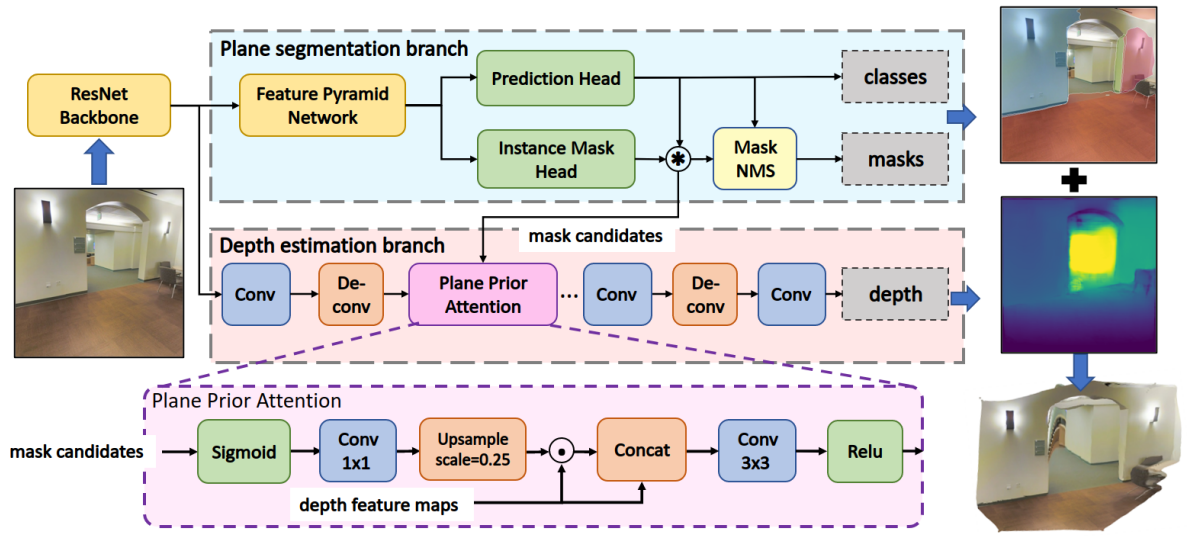

Figure 2.6: The PlaneRecNet Architecture. Taken from the respective paper [50, Figure 1]

.

The entire architecture of PlaneRecNet is portrayed in Figure 2.6. The general approach of this method is to calculate plane parameters through principle component analysis (PCA) or RANSAC after providing a precisely estimated depth. This is achieved by implementing two separate branches, namely *Plane segmentation*, and *Depth estimation*. Both branches obtain their input from a common precursor which is a *ResNet* [17] backbone. The *Plane segmentation* branch is a lightweight configuration of SOLOV2 [49] that has been modified to fit the context of plane detection. The *Depth estimation* branch is a lightweight *Feature Pyramid Network* (FPN) [26]. Within the *Depth estimation* branch, a so-called *Plane Prior Attention* (PPA) module is used to introduce the mask candidates from the *Plane segmentation* branch into the depth estimation. The PPA module is based on the *Depth Attention Volume* [21].

The estimated depth values and the segmentation masks, and classes, are then combined into a piecewise planar scene reconstruction of the input image. No further refinement is implemented.

2.5.12 PlaneRCNN

RCNN [27] is a deep neural architecture that detects planar regions and reconstructs a piecewise planar depth map from RGB-Images.

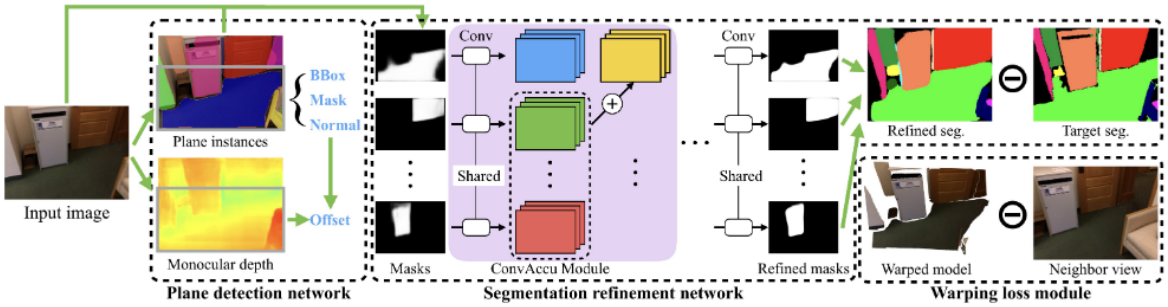

Figure 2.7: The PlaneRCNN Architecture. Taken from the respective paper [27, Figure 2].

The architecture of PlaneRCNN, as seen in Figure 2.7, consists of three primary modules:

1. The plane detection network,
2. a segmentation refinement network, *and*
3. a warping loss module.

The first module is built upon the semantic segmentation network MaskRCNN [16]. The module is modified to differentiate between "planar" and "non-planar" object instances. In contrast to *PlaneNet* (see Subsection 2.5.10), the number of planes to detect is not pre-determined. Moreover, plane parameters and segmentation masks are calculated.

The second module, namely the *segmentation refinement network*, refines the extracted segmentation masks obtained from the *plane detection network*. This is done by introducing non-locality into a U-Net [37] by combining a convolution layer with an accumulation of feature volumes. The authors name this particular step the *ConvAccu* module [27, Section 3.2].

The *warping loss module* implements a refinement step. This module uses a second angle of the same view to ensure consistency. A view from 20 frames ahead is projected into the current view to further refine the segmentation process. It is worth noting, that this is only performed during training to improve the accuracy.

2.6 Datasets

This section outlines a set of datasets popular in the evaluation of algorithms in the field of plane detection. Table 3.3 summarizes the key characteristics of each dataset. The in-

dividual datasets are outlined in the following subsections.

2.6.1 2D-3D-S

2D-3D-S [2] was recorded in three different buildings and divided into six distinct areas, including 272 different scenes. A detailed statistic of the included scene types can be found in Table 4.1. An individual scene has a complete unstructured point cloud and a list of annotated files representing semantically different objects that can be found therein. The dataset includes a wide range of point cloud sizes, with a minimum of $8 \cdot 10^4$ and a maximum of $7 \cdot 10^6$ Furthermore, the average amount of points per scene is $\sim 10^6$ with an average file size of $\sim 34mb$.

2.6.2 Leica

The Leica[5] dataset is a collection of 23 scans of outdoor environments. Each scan consists of a dense unorganized point cloud which has been recorded by the *Leica BLK360* LiDAR Scanner[6]. The dataset is saved in *ASTM E57* [20], which is a general-purpose file format usually used for the storage of 3D data, e.g., point clouds, laser scans or images.

2.6.3 Kinect

The *Kinect* [34] dataset is a set of 30 organized point clouds. The recording was performed, as the dataset's name suggests, with a Microsoft Kinect camera with a 640x480 resolution. A ground truth that focuses on plane and cylinder segmentation is provided in addition to the point clouds.

2.6.4 SYNPEB

The *SYNPEB* dataset was introduced by Schaefer et al. [42] to improve upon the popular *SegComp* dataset. The synthetic dataset includes a 6x7x3m room with various geometric objects inside (see Figure 2.8). Moreover, a total of 40 scans from different views within the room are provided as organized point clouds with a resolution of 500x500. Lastly, the provided ground truth represents a planar segmentation of the scene.

[5] https://shop.leica-geosystems.com/de/leica-blk/blk360/dataset-downloads
[6] https://shop.leica-geosystems.com/de/leica-blk/blk360

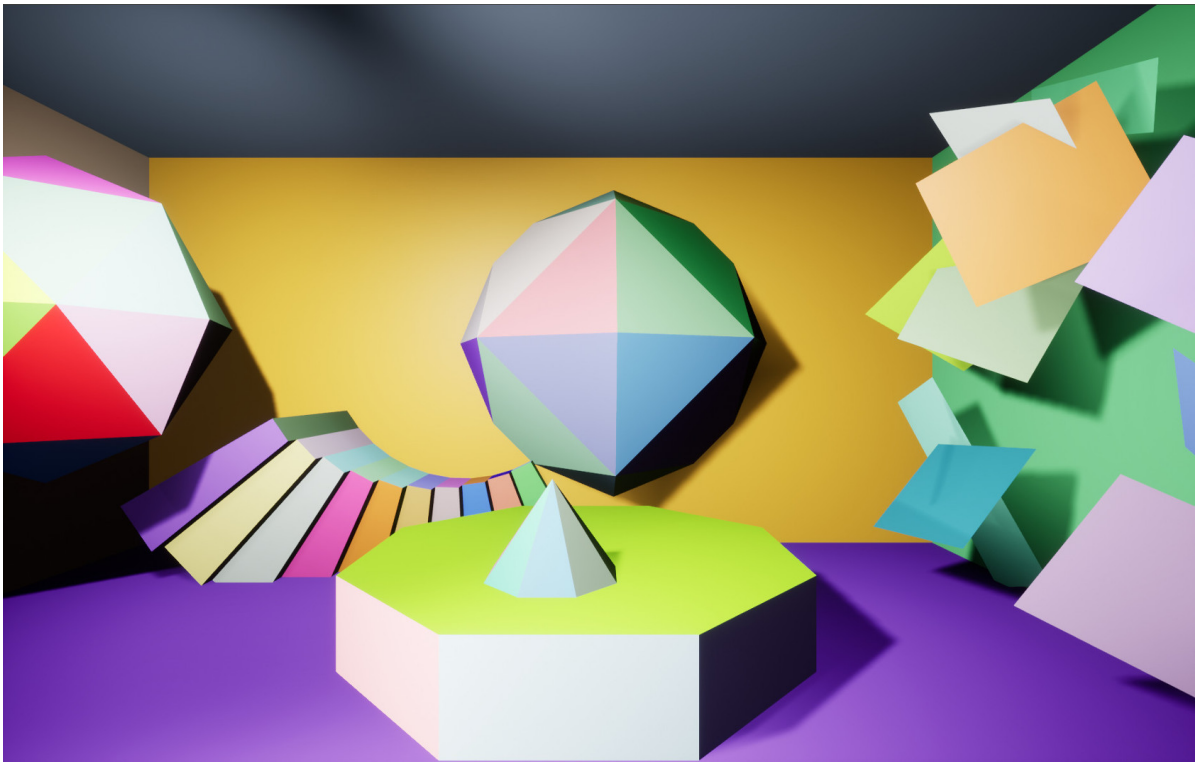

Figure 2.8: The *SYNPEB* room, taken from http://synpeb.cs.uni-freiburg.de/.

2.6.5 ARCO

The *ARCO* [18] dataset consists of 6 organized point clouds that have been recorded with a Microsoft Kinect camera. All scenes show real indoor spaces, including a living room, a kitchen, a saloon, a hallway, furniture, and an ordinary room. They are saved in the popular *.pcd*[7] file format. We are not aware of the existence of a ground truth.

2.6.6 SegComp

The *SegComp* [19] dataset includes a collection of over 400 depth images, as well as a corresponding ground truth. Additionally, a complete evaluation package is provided on the corresponding website[8]. The images are saved in their own file format, namely *gt-seq*.

[7] http://pointclouds.org/documentation/tutorials/pcd_file_format
[8] http://www.eng.usf.edu/cvprg/range/seg-comp/SegComp.html

2.6.7 NYU V2

The *NYU-V2* [43] dataset is an improvement of the preceding version, namely *NYU-V1*[9]. The dataset consists of 1449 RGB-D images, 464 scenes from 3 cities, and more than $400,000$ unlabeled frames. A ground truth in form of labeled objects is provided, as well as a toolbox for arbitrary manipulation of data. Everything was recorded with the Microsoft Kinect camera.

2.6.8 ICL-NUIM

The *ICL-NUIM* [14] dataset was introduced for the benchmarking of RGB-D, VO and SLAM algorithms. Eight scenes are included, which are comprised of a surface ground truth, depth images, and the trajectory of the camera. The dataset includes a total of over 8000 images over these four scenes, whereas four have been recorded two indoor environments, namely a living room, and an office.

2.6.9 SUNRGB-D

The *SUNRGB-D* [44] dataset is used for 3D object detection. The data is split into a training set and a testing set. Over both sets, a total of over $13,000$ RGB-D images are included, with corresponding ground truths in form of 3D bounding boxes. Furthermore, a toolbox is provided. The dataset differentiates between 19 different objects, including, but not limited to: "wall", "door", "bookshelf", and "table". More information can be found on the related website[10] under "Other Materials".

2.6.10 TUM

The *TUM* [45] dataset was created for the evaluation of VO and Visual-SLAM systems. A Microsoft Kinect sensor with a resolution of 640x480 is used to record a total of 39 scenes in indoor environments. While the dataset is primarily focused on trajectories, organized point clouds are provided as well. A ground truth trajectory is provided for each scene. The dataset can be found on the project website [11].

[9] https://cs.nyu.edu/s̃ilberman/datasets/nyu_depth_v1.html
[10] https://rgbd.cs.princeton.edu/challenge.html
[11] .https://vision.in.tum.de/data/datasets/rgbd-dataset/download

2.7 Evaluation Metrics

Wenn man sachen segmentiert oder muster erkennen möchte usw. benutzt man oft zur evaluierung metriken, die die qualität der benutzten methode beschreiben. Usual metrics are *Precision, Recall* and the *F1-Score*. In general, *Precision* describes how many of the results are relevant, i.e., the percentage of correctly calculated values(see Eq. 2.10). *Recall* describes the ratio of relevant results to all relevant data, i.e. the likelihood of a result being relevant(see Eq. 2.11). Lastly, the *F1-Score* is the harmonic mean of the former two metrics (see Eq. 2.12).

$$Precision = \frac{\text{True Positive}}{\text{True Positive + False Positive}} \tag{2.10}$$

$$Recall = \frac{\text{True Positive}}{\text{True Positive + False Negative}} \tag{2.11}$$

$$\textit{F1-Score} = 2 \cdot \frac{Precision \cdot Recall}{Precision + Recall} \tag{2.12}$$

In the context of this work, we calculate *Precision, Recall* and the *F1-Score* as follows. Required are the original point cloud PC, the corresponding list of ground truth planes GT and the planes obtained from a plane detection algorithm A. First, we regularize the PC to reduce complexity and to avoid proximity bias, because of the inverse relationship between distance to sensor and cloud density. This regularization is obtained through voxelization of the point cloud. With this voxel grid, we can now calculate corresponding sets of voxels for each list of points that represent a plane. In the next step, we compare our planes from GT with A to obtain a list of corresponding pairs of ground truth and found planes. A ground truth plane gt_i is marked as *detected* if any plane from the list of found planes achieves a minimum voxel overlap of 50%. With this list of correspondences, we calculate *Precision, Recall* and the *F1-Score*.

For a given ground truth plane gt_j and a corresponding detected plane a_k we can sort a given voxel v_i into the categories *True Positive(TP), False Positive(FP) and False Negative(FN)* as follows.

$$v_i \in gt_j \wedge v_i \in a_k \Rightarrow v_i \in TP$$
$$v_i \in gt_j \wedge v_i \notin a_k \Rightarrow v_i \in FN$$
$$v_i \notin gt_j \wedge v_i \in a_k \Rightarrow v_i \in FP$$

With those rules, we can calculate the Precision, Recall and F1 score like this:

$$Precision = \frac{|TP|}{|TP| + |FP|}$$

$$Recall = \frac{|TP|}{|TP| + |FN|}$$

3 Concept

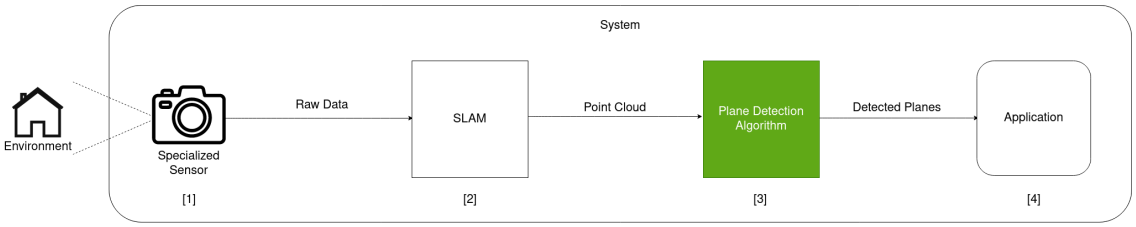

Figure 3.1: The procedure of the plane detection process. The specialized sensor records data ([1]), which is passed to a SLAM algorithm ([2]). After map assembly, a point cloud is handed to a plane detection algorithm ([3]). The detected planes are given to a use-case-specific application ([4]).

Many AR and VR Systems integrate plane detection into their software, some use it only to calculate the ground floor while others use plane detection to build a smaller model of the environment. Figure 3.1 shows a generic block diagram of such a VR/AR system including plane detection. In general, the environment is continuously recorded by a specialized sensor which is usually a camera([1]). A SLAM algorithm then integrates the new data into its already existing map([2]). The map, in form of a point cloud, is subsequently passed to a plane detection algorithm([3]). The algorithm performs the necessary steps to detect all planes inside the current map and passes the planes to the application([4]). The application would then further process those planes, e.g., by creating a live visualization of them or by assisting the movement of visually impaired people [7].

To remove any noticeable delay in the application, the plane detection step has to run under a temporal restriction, henceforth referred to as *real-time*. We introduce a thorough definition of *real-time* in Section 3.3.

When creating such an AR/VR system, the choice of plane detection algorithm is naturally of great importance. The problem is that most published algorithms are inherently incomparable. Often different datasets or metrics are used, which precludes comparison by quantification. Alternatively, algorithms are not comparable by internal functionality because many methods require other inputs, and the format of the planes differs

accordingly. All in all, selecting a single 'best' algorithm, solely based on the results presented in their respective work, is impossible.

To answer the question of which algorithm is best and whether it is real-time capable, we make a unified comparison of plane detection algorithms. To perform this evaluation, we need the following:

1. Appropriate plane detection algorithms,
2. a useful dataset, *and*
3. a definition of *real-time*.

The following sections are dedicated to these requirements.

3.1 Selection of Plane Detection Algorithms

Since most algorithms differ in certain aspects, it is not possible to compare them all uniformly. Furthermore, not all algorithms are created out of the same motivation and, therefore, focus on different things. Evaluating an algorithm in a scenario it has not been designed for would not yield meaningful results. It is, therefore, necessary to first define objective criteria to superficially determine which algorithm seems to be relevant for the context of this work.

3.1.1 Criteria

In the following paragraphs, we outline appropriate criteria for the objective assessment of plane detection algorithms.

Type of Input The first criterion is the type of input expected by a plane detection algorithm. Allowing vastly different input types is likely to render the evaluation more complicated, if not impossible because an equivalent transformation between two input types is not always possible.

We detail the different types of input in Section 2.3. To reiterate, the data representation of the recorded environment falls into one of three categories:

- *unorganized* or *unstructured point cloud* (UPC)
- *organized* or *structured point cloud* (OPC)
- image:

– Depth (DI)

– RGB (RGBI)

OPC and UPC both describe point clouds in the cartesian coordinate system. The primary difference is that the 3D coordinates inside an *organized* point cloud are saved in a 2D grid, while the *unorganized* point cloud resembles an unsorted 1D array.
Like OPC, depth images are a 2D grid of values. However, in contrast to the 3D coordinates of an OPC, the data points of depth images are the distances to the sensor.

Detected Plane Format Which specific representation the detected planes take the form of is also essential. If no uniform output type can be determined, consequently, no uniform metric for comparison can also be found.

Often the found planes are saved as a list of 3D points, henceforth referred to as inliers, which were assigned to a plane. Another often used plane output format is the cartesian equation of a plane described by a normal vector n and a vector d.

In methods that work on image data, found planes are often described by a segmentation mask (SM) or regions of pixels that belong together.

Finally, some methods use plane detection as a means to an end, e.g., for the reconstruction of a scene or the integration into a SLAM architecture.

Hardware Requirements Another important aspect to consider is the hardware required by an algorithm. Many applications in the field of robotics are limited in their processing power, often restricted to microcontrollers like a Raspberry Pi[1] or an Arduino[2]. Thus, most plane detection algorithms run on the *CPU*, while some even implement some form of *CPU* parallelism, e.g., 3D-KHT uses OpenMP[3] to speed up the octree construction [25, Section 4]. However, some methods are implemented either completely or partially on the *GPU*. For instance, Hidalgo-Paniagua et al. [18] compare different implementations of the RANSAC algorithm, whereas three versions are processed entirely on the *CPU*, and the last one is offloaded to the *GPU* via CUDA[4].

To summarize, we differentiate between algorithms that run solely on the *CPU* and algorithms that, additionally, employ the machine's *GPU*.

[1] https://www.raspberrypi.com/
[2] https://www.arduino.cc/
[3] https://www.openmp.org/
[4] https://developer.nvidia.com/cuda-toolkit

Availability Lastly, to use an algorithm, one has to be able to implement it. Some implementations are published alongside the corresponding paper. Moreover, the availability of an implementation may be restricted by certain legalities. While other publications are limited to the paper, the level of detail regarding the implementation details varies.

For further reference, we consider a plane detection algorithm to be *available* if its implementation is successful, and that the implementation does not involve a form of legal transaction. **die formulierung muss im grund aussagen, dass man seine seele nicht verkaufen muss um da ran zu kommen, dh im zweifel selber impl können, oder eine geg. nehmen. PEAC: formular ausfüllen wäre ne grauzone, aber daten sind ja kein geld oder? :') dementsprechend sicher stellen dass die Y/N richtig sind**

3.1.2 Plane Detection Algorithms

irgendwas zu "das ist logischerweise nicht alles, aber algorithmen die minuten brauchen haben wir gekonnt ignoriert" A list of state-of-the-art algorithms is compiled through comprehensive research of the current literature on plane detection (see Table 3.1). The table shows the input type and the output format of all algorithms, as well as the required hardware, and the availability. Note, that we consider all algorithms to be available, however, we are not aware of public implementations of OBRG and SCH-RG. However, the respective publications outline their methods in high detail, thereby guiding a re-implementation.

PEAC?

The final output of *PLaneNet, PlaneRecNet* and *PlaneRCNN* is a piecewise-planar depth map of the input image. Since modifying the architecture to return the segmentation masks and plane parameters would require minimal effort, we adjusted the output types in the table accordingly. Similarly, *RSPD* returns a set of planes parameterized by its normal vector n, distance to origin d, and two additional extents. Modifying the output to return inliers requires minimal effort as well.

Plane Detection Algorithm	Input Data	Plane Format	Hardware	Available	Section
RSPD [1]	UPC	3D-IN, (n, d)	CPU	Y	2.5.1
OPS [46]	UPC	3D-IN	CPU	Y	2.5.2
3DKHT [25]	UPC	3D-IN	CPU	Y	2.5.3
OBRG [48]	UPC	3D-IN	CPU	Y	2.5.4
PEAC [12]	OPC	2D-IN	CPU	Y	2.5.5
CAPE [36]	OPC	(n, d)	CPU	Y	2.5.6
SCH-RG [31]	OPC	2D-IN	GPU	Y	2.5.7
D-KHT [47]	DI	2D-IN	CPU	Y	2.5.8
DDFF [40]	DI	2D-IN	CPU	Y	2.5.9
PlaneNet [28]	RGBI	2D-IN, (n, d)	GPU	Y	2.5.10
PlaneRecNet [50]	RGBI	2D-IN, (n)	GPU	Y	2.5.11
PlaneRCNN [27]	RGBI	2D-IN, (n, d)	GPU	Y	2.5.12

Table 3.1: A list of Plane Detection Algorithms compiled by reviewing the current literature. The algorithms are clustered by their type of input. The rightmost column provides the placement within this work. We refer to Subsection 3.1.1 for details regarding the specific namings.

As mentioned above, we consider all presented algorithms available even if *SCH-RG* and *OBRG* do not seem to have an official implementation. Therefore, while necessary, the *availability* criterion does not constrain the selection of algorithms in this case.

As stated in Paragraph 3.1.1, mobile robotics applications or AR/VR systems are often limited in their processing power. Moreover, integrating an external GPU into the system poses an additional cost factor. We exclude algorithms that require an external GPU, namely *SCH-RG, PlaneNet, PlaneRecNet*, and *PlaneRCNN*.

Addressing the criterion of *input type*, we are only interested in performing plane detection in complete environments. Each update published by RTAB-MAP is the union of new data and the current state of the recorded map. RTAB-MAP publishes this update in form of an *unorganized* point cloud (see Figure 2.1). To perform plane detection with an algorithm that expects an *organized* point cloud as input, the UPC has to be transformed into an OPC. This transformation is not-trivial and involves the projection of 3D coordinates onto a sphere based on a set of sensor parameters. An exemplary implementation thereof is included in the lidar toolbox of MATLAB[5]. However, this transformation neglects the global structure of the environment, as it returns a two-dimensional representation of the environment. Therefore, we focus on *unorganized* point clouds in this work and exclude *PEAC, CAPE, SCH-RG, D-KHT, DDFF, PlaneNet, PlaneRecNet* and *PlaneRCNN* from our evaluation.

The detected planes need to be in the same format because, even for the same plane, different representations could very well lead to different results. Assume a plane in

[5]https://de.mathworks.com/help/lidar/ug/unorgaized-to-organized-pointcloud-conversion.html

cartesian form (n, d) and a plane represented by its inliers (3D/2D). The calculated metrics may differ significantly because the plane in cartesian form is infinitely dense. Conversely, the plane described by its inliers allows for holes and non-rectangular shapes, e.g., doorways or a round table, respectively. Being able to represent planes of any shape is important for many applications. Moreover, only the 3D inliers $3D - IN$ conform to the determined input type of UPC (see Section 2.3.2). We thereby determine *three-dimensional inliers* (3D-IN) as the preferred *plane format* and exclude all methods which do not comply, namely *CAPE, PlaneNet, PlaneRecNet*, and *PlaneR-CNN*.

Note, that 3D inliers are henceforth referred to solely as *inliers*.

Applying these restrictions, we end up with, and thus include, the following plane detection algorithms in our evaluation:

- **RSPD**
- **OPS**
- **3D-KHT**
- **OBRG**

Temporal Subdivision in Phases To enable a precise evaluation, we subdivide these plane detection algorithms into three phases: The pre-processing phase, the plane detection phase, and the post-processing phase. Note, that we use the terms "phase" and "step" interchangeably in this work. In the following, we outline the pre-processing and post-processing steps taken by the selected algorithms. To avoid redundancy, we refer the reader to the Subsections 2.5.1-2.5.4 for a detailed explanation of each algorithm.

The pre-and post-processing steps are summarized in Table 3.2. RSPD, 3D-KHT, and OBRG construct an octree (OC) during their pre-processing phase. Additionally, RSPD and OBRG perform an initial estimation of normals (NE). OPS estimates the normal vectors for a randomly chosen sample set of points of pre-determined size.

During post-processing, OPS merges smaller planes if they pass a coplanarity test and then re-estimates the normals of the resulting plane. In the post-processing step, OBRG refines the borders of detected planes by inserting previously unallocated regions. RSPD and 3D-KHT do not perform post-processing.

	RSPD	OPS	3D-KHT	OBRG
Pre	NE	NE	OC	OC + NE
Post	/	Merge	/	Refinement

Table 3.2: The Pre-processing and post-processing steps of the plane detection algorithms. "/" denotes the absence of a pre-/post-processing step.

3.2 Datasets

As mentioned at the beginning of this chapter, we also need an appropriate dataset for the evaluation. Through extensive research of current literature, we compiled a list of popular datasets (see Table 3.3).

Dataset	Scene Format	Real	Indoor	GT	Section
2D-3D-S [2]	UPC	Y	Y	objects	2.6.1
Leica[6]	UPC	Y	N	planes	2.6.2
Kinect [34]	OPC	Y	Y	planes	2.6.3
SYNPEB [42]	OPC	N	/	planes	2.6.4
ARCO [18]	OPC	Y	Y	/	2.6.5
SegComp [19]	DI	N	/	planes	2.6.6
NYU V2 [43]	DI	Y	Y	classes	2.6.7
ICL-NUIM [13]	DI	Y	Y	trajectory	2.6.8
SUNRGB-D [44]	DI	Y	Y	objects	2.6.9
TUM [45]	DI	Y	Y	trajectory	2.6.10
FIN (ours)	UPC	Y	Y	planes	4.4

Table 3.3: Plane detection Datasets. The GT(Ground Truth) column specifies what the ground truth of each dataset represents. Note, that the synthetic datasets (e.g., SegComp and SYNPEB) represent neither indoor nor outdoor scenes, hence the "/" in the respective table entries. The datasets are clustered by their type of format. Moreover, the remaining order is arbitrary. The rightmost column provides the placement within this work. Note, that we include our dataset (FIN) in this table for completeness reasons.

In Subsection 3.1.2, we determine *unorganized* point clouds as the type of input. Furthermore, we focus on plane detection in real environments in this work. Because most datasets do not conform to these two requirements, only *2D-3D-S* and *Leica* remain.

[6]https://shop.leica-geosystems.com/de/leica-blk/blk360/dataset-downloads

Since we focus on plane detection in indoor environments, *Leica* ceases to be an option. Thus, we choose *2D-3D-S* as the dataset for the evaluation.

Nonetheless, we cannot use the provided ground truth of *2D-3D-S* because it represents the segmented scene on the level of objects, rather than planes in the scene. Consequently, we create an appropriate ground truth by manual segmentation of all planes in a given scene. We outline the details thereof in Section 4.3.

Lastly, *2D-3D-S* does not inherit any temporal component, i.e., the *unorganized* point clouds do not grow incrementally over time. To the best of our knowledge, there exists no dataset that meets the above criteria and, additionally, provides a plane-focused ground truth. Therefore, we record an incrementally growing dataset in the Faculty of Computer Science at Otto-von-Guericke University Magdeburg, henceforth referred to as the *FIN* dataset.

To perform a thorough comparison between the *FIN* and *2D-3D-S*, and, subsequently, between the static and the dynamic dataset, we record a scene for each of the following scene types:

- office
- conference room
- auditorium
- hallway

We focus on these four scene types because they are the most common in a real indoor environment. The recorded point clouds can be seen in Figure 3.2. Lastly, since this is a novel dataset and thus has no ground truth, we create a ground truth. The details thereof are explained in Section 4.4.

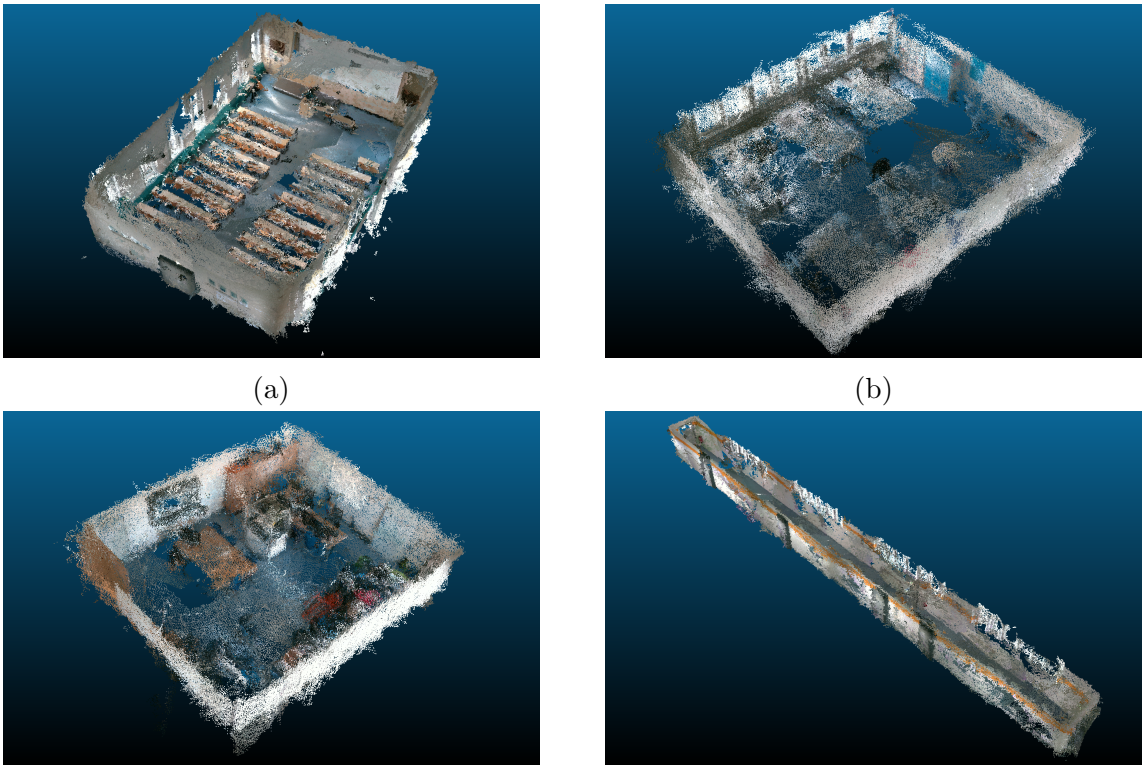

(a) (b) (c) (d)

Figure 3.2: The recorded point clouds for each scene type: (a) auditorium, (b) conference room, (c) office and (d) hallway. The ceilings have been manually removed for visualization purposes but remain in the dataset for the experiments.

3.3 Definition Real-Time

Finally, as mentioned in Section 3, to determine whether or not an algorithm runs in real-time, we must first define the meaning of real-time.

In Subsection 3.1.2, we introduce the differentiation between pre-processing and post-processing steps. It is possible that one phase of an algorithm accounts for the majority of the total calculation time and that the algorithm would be considered *real-time* applicable, if that phase were to be excluded. Because some steps can be covered by previous steps in the AR/VR system (see Figure 3.1), i.e., by the sensor or the SLAM algorithm, we give two definitions of *real-time*.

In general, and without taking the algorithms internal structure into consideration, we have to consider possible hardware limitations, data flow, and how often it is needed to

perform calculations, e.g., how quickly the SLAM algorithm updates the map (Figure 3.1, [2]) or how frequent new planes are needed (Figure 3.1, [4]).

The recorded raw data is not directly sent to the plane detection algorithm but instead given to RTAB-MAP, which then performs calculations to update and publish the map. Therefore, the upper limit is the frequency of how often RTAB-MAP publishes those updates, which by default is once per second.

Total Real-Time RT_{tot} According to this upper limit of RTAB-MAP, we consider an algorithm *totally Real-Time* applicable, if it achieves an average frame rate of minimum 1, e.g., the total processing time of an algorithm lies under one second. In the remainder of this work, we use *total Real-Time* and RT_{tot} interchangeably.

Real-Time Plane Calculation RT_{calc} Being a subset of *totally Real-Time applicability, Real-Time Plane Calculation* determines the real-time applicability if the processing time of an algorithm *excluding* pre-processing lies under the aforementioned upper bound of $1s$. Like RT_{tot}, we use *Real-Time Plane Calculation* and RT_{calc} interchangeably.

3.4 Summary

Many applications have constraints in the form of a temporal component. Augmented or Virtual Reality applications that include plane detection are no exception. In addition to time constraints, good quality is usually tightly coupled to expensive sensors. In this work, we aim to evaluate the quality of real-time plane detection algorithms under the use of more affordable hardware, i.e., Intel RealSense. At the beginning of this chapter, we state that three aspects are required for this evaluation, namely plane detection algorithms, a dataset, and a definition of real-time. The selection of the best plane detection algorithm, however, is non-trivial. After defining meaningful criteria for objective judgement, we select appropriate plane detection algorithms. Moreover, we select two datasets, one of which is a novel creation, and present two definitions of *real-time* namely RT_{tot} and RT_{calc}. In Chapter 5, we perform the evaluation.

4 Implementation

This chapter provides the implementation details of the outlined concept of the previous chapter.

4.1 System Setup

It is necessary to perform all experiments on the same machine to ensure a consistent comparison. We implement all algorithms and further architecture on a Lenovo IdeaPad 5 Pro, which runs Linux Ubuntu 20.04.5. The laptop has an AMD Ryzen 7 5800H CPU and 16 GB of RAM.

We install the most recent ROS distribution, *ROS Noetic Ninjemys*[1], as well as *realsense-ros*[2] with all additional dependencies. Note, that the version of *realsense-ros* changed over the course of this work.

4.2 Plane Detection Algorithms

In Chapter 2, we provide detailed information about the algorithms we select in Section 3.1. The following subsections deal with the implementation details thereof. Note, that the subsections of RSPD and OPS are joined due to a lack of noticeable difference in implementation details.

4.2.1 RSPD & OPS

We implement RSPD[3] and OPS[4] using their respective open source implementations on GitHub. Note that, while the implementation of RSPD is provided by one of the authors, we could not determine whether the user who uploaded his implementation

[1] http://wiki.ros.org/noetic
[2] https://github.com/IntelRealSense/realsense-ros/tree/ros1-legacy
[3] https://github.com/abnerrjo/PlaneDetection
[4] https://github.com/victor-amblard/OrientedPointSampling

of OPS is affiliated with Sun and Mordohai[46]. Both methods are implemented in C++ and depend on the C++ linear algebra library *Eigen*[5], and the C++ API of the Point-Cloud Library [41], *libpcl-dev*.

4.2.2 3D-KHT

The authors of 3D-KHT, provide an implementation, in form of a Visual Studio project, on their website[6]. Since the laptop we use does not run Windows, we use *cmake-converter*[7] to convert the solution to a CMake project we can build using *make*. The dependencies of this implementation include the C++ library *Dlib* [23], as well as the OpenGL Utility Toolkit *GLUT*[8]. Lastly, the multi-processing API OpenMP[9] is required as well.

4.2.3 OBRG

To our knowledge, no open-source implementation is available for the algorithm. We, therefore, use our own implementation, which can be found on our Github repository[10].

We implement the algorithm using python. We choose to write our own octree implementation for spatial subdivision of our point cloud, since the implementation of public libraries like *open3d* [53] are limited in terms of leaf node functionality. The subdivision is followed by calculating the saliency features using *open3d*'s normal estimation function. We follow the pseudocode as stated in [48, Algorithm 1]. We modify the insertion into the set of regions by adding a containment check, to avoid redundancy of regions. By reducing the number of regions (incl. redundancies), we also reduce the total calculation time.

4.3 2D-3D-S

The *2D-3D-S* dataset provides a ground truth in form of annotated point clouds corresponding to 13 object classes. Since these annotated objects are not always planar, we cannot use them for the evaluation of plane detection algorithms. Thus, we create a

[5]https://eigen.tuxfamily.org/index.php
[6]https://www.inf.ufrgs.br/ oliveira/pubs_files/HT3D/HT3D_page.html
[7]https://cmakeconverter.readthedocs.io/
[8]https://www.opengl.org/resources/libraries/glut/glut_downloads.php
[9]https://www.openmp.org/
[10]https://github.com/lupeterm/OBRG

ground truth that focuses on planar structures. We use the open-source 3D point cloud and mesh processing software *CloudCompare*[11] to visualize a scene and manually segment included planes. Because we cannot assume all walls to be planar or that, e.g., the tops or three adjacent tables always form the same number of planes (see Figure 4.1b), we have to view each point cloud and segment the included planes manually. An exemplary before- and after-segmentation is shown below in Figure 4.1a.

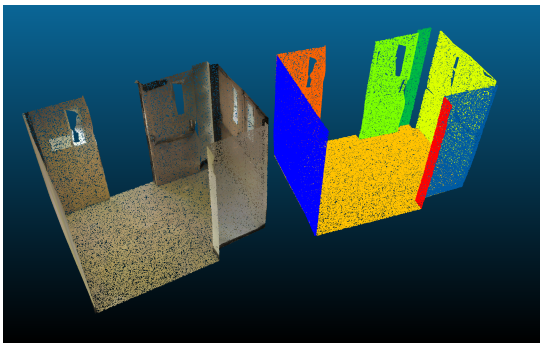

(a) Ground Truth Segmentation of a hallway in CloudCompare. Shown is the input cloud on the left and segmented planes on the right. Both are cropped and without ceilings for visualization purposes.

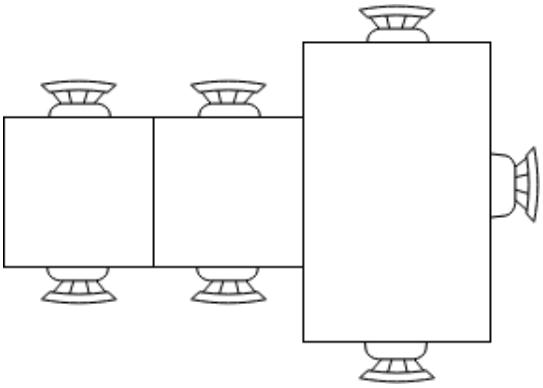

(b) The provided ground truth considers these tables to be three separate objects. Within the context of plane detection, the three table tops would form exactly one plane.

Figure 4.1

The manual segmentation process is very time consuming, not only because of the large amount of data but also due to the level of subjectivity involved. On average, the segmentation of a scene took 8-10 minutes, which, for all 272 scenes, would result in a total of 36-45 hours. To reduce the time spent in segmentation, we perform an initial analysis of the scenes in a given area and omit scenes that show no noticeable difference compared to others. This analysis reduces the number of segmented scenes to slightly more than half of the total, reducing the time to 18-23 hours.

The results of the manual segmentation process are documented in Table 4.1. The table is inspired by [2, Table 7]. Like the original, it shows the amounts of scenes per scene type in each area. We extended the table by adding a column dedicated to the planes included in each scene type. According to the table, a total amount of 3410 planes are included in the dataset.

[11] https://www.danielgm.net/cc/

Scene Categories	Area_1	Area_2	Area_3	Area_4	Area_5	Area_6	TOTAL	Planes
auditorium	-	2/2	-	-	-	-	2/2	70
conference room	2/2	1/1	1 /1	3/3	3/3	1/1	11/11	375
copy room	1/1	-	-	-	-	1/1	2/2	45
hallway	8/8	12/12	6/6	14/14	1/15	6/6	48/61	977
lobby	-	-	-	2 /2	1/1	-	3/3	207
lounge	-	-	2/2	-	-	1/1	3/3	101
office	16/31	5/14	10/10	9/22	4/42	3/37	48/156	1116
open space	-	-	-	-	-	1 /1	1/1	10
pantry	1/1	-	-	-	/1	1/1	3/3	73
storage	-	9/9	2 /2	4/4	4/4	-	19/19	222
WC	1/1	2/2	2/2	4/4	4/2	-	11/11	214
							139/272	**3410**

Table 4.1: 2D-3D-S dataset statistics. Shown are the number of scenes per category and for how many we created a ground truth ($\#GT/\#Total$). Note, that the rightmost column reports the number of segmented planes per scene category and does *not* correspond to other columns in this table.

4.4 FIN Dataset

Reiterating Section 3.2, we select four scene types of the *2D-3D-S* dataset for the recording of the self-created FIN dataset. Namely, these scene types are *auditorium, conference room, hallway,* and *office*. All scenes are recorded inside the *Faculty of INformatik* (FIN) at Otto-von-Guericke-University in Magdeburg. Running *realsense-ros* and holding our cameras, we walk through the corresponding parts of the building while scanning to the best of our ability. We save each incremental map update to a file for further usage.

Given the differences in spatial dimension, the recordings of each scene also differ in length and size. The auditorium scene has a total of 296 individual time frames, the conference room scene has 113, the hallway has a total of 174, and the office has 125 time frames. The FIN dataset, thereby, has a total of 708 time frames.

Since no ground truth exists for a novel dataset like this, we create a set of ground truth planes gt_{end} for only the most recent update of each scene, e.g., for the entire recording. By creating a ground truth for only the last frame of each scene, we substantially reduce the time invested in this task. To prepare for the evaluation of a point cloud m_t at a given time t, we crop all planes in gt_{end} by removing all points that are not present in m_t. Figure 4.2 shows the final point cloud and the manually created ground truth gt_{end} of the *hallway* scene on the far right. On the left thereof, two point clouds of earlier stages of the recording are shown, as well as their dynamically created ground truth.

We speed up this expensive process by employing a KD-Tree neighbor search with a small search radius since we only need to know whether a certain point is present or not.

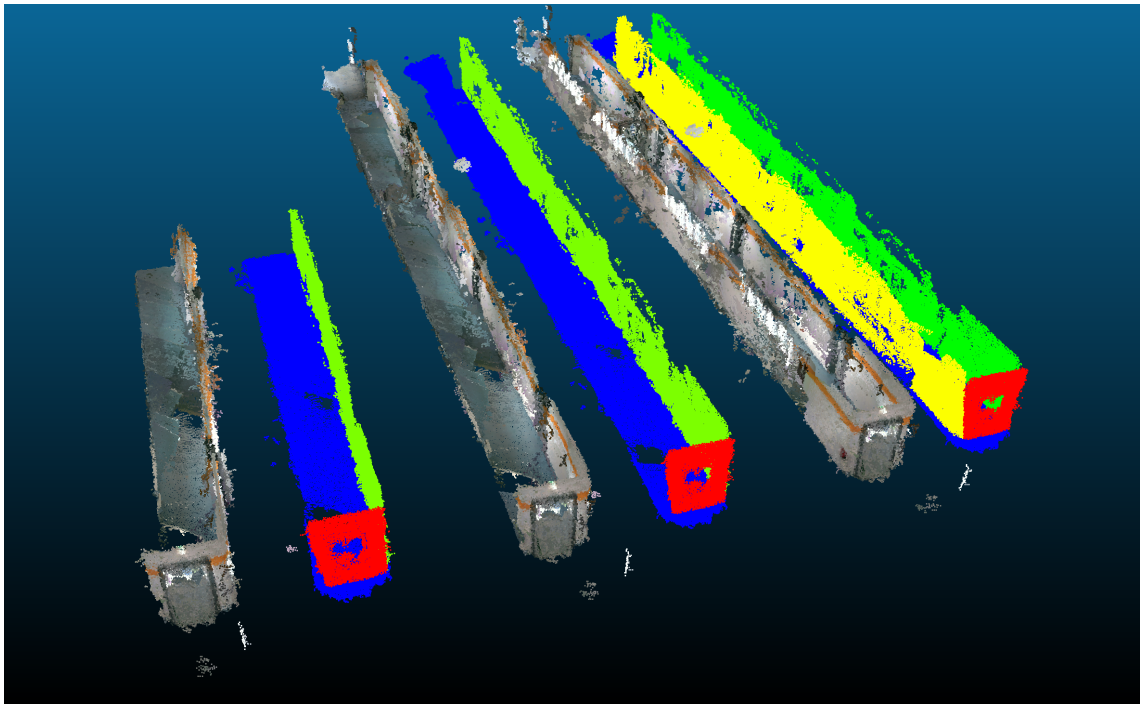

Figure 4.2: Dynamic ground truth generation shown by the example of three point clouds from the *hallway* scene, as well as the corresponding ground truth. The rightmost pair shows the final state of the point cloud and its ground truth.

5 Evaluation

In this chapter, the previously selected algorithms are uniformly compared. We present and analyze the results. Prior to the evaluation, we present the protocol thereof.

5.1 Protocol

This work aims to determine which plane detection algorithm is the most suitable for an AR/VR system. For this decision, we uniformly compare the algorithms selected in Chapter 3. We split the comparison into two experiments conducted on different datasets: the *2D-3D-S* and the self-created *FIN* dataset. We conduct both experiments on an AMD Ryzen 7 5800H CPU with 16GB of RAM. Since both datasets are fundamentally different, we will perform the experiments and the analysis separately and then compare the results. First, we present the metrics used for comparison, followed by an outline of the used configurations of parameters for each experiment.

5.1.1 Metrics

The following two paragraphs detail the metrics we use in this evaluation. Note, that by using the term "time frame t" or "time step t", we refer to the state of the point cloud at a given time t.

Accuracy To quantify the accuracy of the plane detection algorithms, we use the detected planes and the created ground truth to calculate the three following metrics: Precision, *Recall*, and the F1-Score. We calculate the *Precision*, as this reports the percentage of correctly detected points within the planes an algorithm returned. Similarly, we calculate the *Recall* because it gives information about the percentage of correctly detected points in comparison to the number of points that *could* be detected. Using these metrics separately is problematic as we cannot expect the distribution of "plane" to "non-plane" to be even. The *F1-Score* is the harmonic mean of the *Precision* and the *Recall* and therefore measures the balance between the *Precision* and *Recall*. Intuitively,

this means that an algorithmhas to yield sufficient *Precision* and *Recall* results to score a sufficient *F1-Score*. The *F1-Score*, thereby, is the primary metric for the quantitative comparison of algorithms in this work. However, we report the *Precision* and the *Recall* for thorough analysis. The procedure of calculation is taken from [1, Section 4] and detailed in Section 2.7. Note that we use the detected planes for the calculation, however, we are not using them directly as a measure of performance due to the subjective nature of manual ground truth segmentation.

Time Measurements In addition to the accuracy, we are interested in the real-time applicability of an algorithm. We introduce two definitions of *real-time* in Section 3.3. To reiterate, we consider an algorithm to be *totally real-time* (RT_{tot}) applicable if its total runtime is smaller than $1s$. Furthermore, we consider an algorithm to achieve *real-time plane detection* (RT_{calc}) if the total calculation time excluding the pre-processing step runs faster than $1s$.

A simple approach to measuring calculation times could involve reporting the average total calculation time over a dataset. However, when recording a real environment, the point clouds likely grow incrementally with each map update. Therefore, the average calculation time alone is of limited significance, as we expect shorter times for the start of a recording and longer times for the most recent point cloud. Based on this assumption, it is necessary to analyze the relationship between the point cloud size and the calculation time as well.

Following the separation of algorithms into phases (see Section 3.1.2), we divide the calculation time into the pre-processing time t_{pre}, the time spent during plane detection t_{calc}, and the duration of post-processing steps t_{post}. This separation enables an in-depth analysis of both average results and the results per time frame. Since we have two definitions of real-time, we introduce two metrics of calculation time:

1. Focusing on t_{calc} and t_{post} allows us to determine whether an algorithm is *real-time plane detection* applicable, *and*
2. to determine whether an algorithm is *totally real-time* applicable, we consider the total computation time t_{tot}, which is the sum of the individual times:

$$t_{tot} = t_{pre} + t_{calc} + t_{post} \tag{5.1}$$

5.1.2 Parameterization of Algorithms

Because the datasets inherit different amounts of noise, it is necessary to modify the algorithms accordingly. We thereby modify the algorithms' parameterization to achieve

more noise robustness. In the following, the parameterizations of the algorithms with respect to the two experiments are outlined. Therein, we refer to the parameterization of the *2D-3D-S* experiment as the default configuration. Furthermore, we determine an appropriate parameterization for the FIN dataset through empirical experiments. These experiments include multiple tests of different combinations of values on all scenes of the FIN dataset, the ranges of which are specified in the respective paragraph of each algorithm.

5.1.2.1 RSPD

Experiment	l_O	ε	MOR	k	MND	MDP
2D-3D-S	10	30	25%	30	60°	0.258
FIN	10	30	25%	30	60°	0.258

Table 5.1: Parameter configuration of RSPD used for the experiments.

2D-3D-S For the *2D-3D-S* experiment, we use the parameters of the provided implementation[1]. These parameters include the maximum octree level l_O, the minimum number of samples per leaf node ε, the Maximum Outlier Ratio MOR per plane, the size of the nearest neighborhood k, the Maximum Normal Deviation MND, and the Maximum Distance to Plane MDP. Note that while $k = 50$ is used in the respective paper [1, Section 3.3], $k = 30$ is used in the official implementation. We adopted the latter because, in our experience, it produces sufficient results while reducing the pre-processing time.

FIN Multiple experiments with different values had been conducted. The individual ranges are $l_O \in [8, 12], \varepsilon \in [15, 150], MOR \in [15, 40], k \in [30, 90], MND \in [50, 70]$, and $MDP \in [0.15, 0.4]$. Through these experiments, we were not able to find a configuration that yields considerably better results than the default parameterization. Therefore, no parameter modifications for the FIN dataset are made.

5.1.2.2 OPS

Experiment	α_s	KNN	θ_h	θ_N	p
2D-3D-S	3%	30	0.05	100	0.99
FIN	3%	**90**	**0.35**	100	0.99

Table 5.2: Parameter configuration of OPS used for the experiments.

[1] https://github.com/abnerrjo/PlaneDetection

2D-3D-S The parameter configuration used for the *2D-3D-S* experiment is shown in the first row of Table 5.2. Like the parameterization of RSPD, we took this configuration from the provided implementation[2]. We use a sampling rate α_s of 3% and a neighborhood size KNN of 30 for the estimation of normal vectors. Additionally, we use a distance threshold θ_h of 0.05(m). Furthermore, we set the inlier threshold θ_N to 100 and the probability for adaptively determining RANSAC iterations p to 0.99, as proposed in [46, Section 4A].

FIN We ran experiments on the FIN dataset with different parameter values in the respective ranges: $\alpha \in [0.3\%, 6\%]$, $KNN \in [30, 150]$, $\theta_h \in [0.05, 0.5]$, $\theta_N \in [50, 1000]$, and $p \in [0.90, 1.0]$. We choose the configuration, that shows a balance between speed and accuracy, namely the following. We increase KNN to 90, as larger neighborhood sizes increase the accuracy of normal estimation and, consequently, the overall accuracy of a method. Furthermore, we increase the tolerated plane thickness θ_h because an increase in sensor noise ultimately thickens the recorded planes. Both modifications are highlighted in bold in the second row of Table 5.2.

5.1.2.3 3D-KHT

Experiment	ϕ_{num}	ρ_{num}	s_{level}	s_{ps}	s_α	s_β
2D-3D-S	30	200	2	0.002	18	6
FIN	30	**100**	2	0.002	**8**	6

Table 5.3: Parameter configuration of 3D-KHT used for the experiments.

2D-3D-S The parameter configuration is shown in Table 5.3. We use an accumulator discretization of 30 and 200 for ϕ and ρ, respectively. Starting to check for planarity at an octree level s_{level} of 2 seems to yield the best results. Limberger and Oliveira[25] propose a minimum of 30 samples per cluster s_{ps}, however, we use 0.2% of the total point cloud due to the wide ranges of point cloud sizes in the dataset (see Subsection 2.6.1). Lastly, we set the plane isotropy tolerance s_β to 6, as proposed in [25, Section 3.1]. In contrast, using a plane thickness tolerance s_α value of 18 seemed to yield better results than the proposed 25. This was determined by a small set of experiments with s_α values ranging between 15 and 33.

[2]https://github.com/victor-amblard/OrientedPointSampling

FIN For the FIN experiment, we modify the values of ρ_{num}, and s_α to accommodate for the higher levels of noise. These values are obtained by performing tests with different parameterizations. Precisely, we used the following parameter ranges combinations of values therein: $\phi_{num} \in [20, 100]$, $\rho_{num} \in [50, 600]$, $s_{level} \in [1, 5]$, $\theta_N \in [50, 1000]$, $s_\alpha \in [5, 23]$, and $s_\beta \in [4, 8]$. Reducing ρ_{num} should decrease the accuracy, however, it seems to yield better results in a high-noise environment like the FIN dataset. We decrease s_α to allow for slightly thicker, e.g. noisier, planes to be detected. The modification of parameters is highlighted in bold in Table 5.3.

5.1.2.4 OBRG

Experiment	l_{max}	θ_{res}	θ_d	θ_{ang}	θ_M	θ_p
2D-3D-S	5	0.08	0.08	0.18	5000	90%
FIN	5	**0.22**	**0.2**	**0.2**	5000	**70%**

Table 5.4: Parameter configuration of OBRG used for the experiments.

2D-3D-S The used configurations for the experiments are shown in Table 5.4. Since the specific values of The parameterization was determined during the implementation process and showed a reasonable compromise between efficiency and accuracy. Due to the low level of noise, we assign a very small tolerance to the residual threshold θ_{res} and the distance threshold θ_d. Additionally, we assign a high planarity threshold value of $\theta_p = 90\%$.

FIN We performed tests with different parameterizations, individually ranging as follows. $l_{max} \in [4\%, 7\%]$, $\theta_{res} \in [0.05, 0.3]$, $\theta_d \in [0.05, 0.3]$, $\theta_{ang} \in [0.13, 0.3], \theta_M \in [200, 6000]$, and $\theta_p \in [70, 90]$. Due to higher levels of noise, and thus, thicker walls, we increase θ_{res}, θ_d, and the angular divergence threshold θ_{ang}. According to [48, Section 3.4], the planarity threshold θ_p should be chosen between 70% and 90% depending on the noise level. As the expected noise level of the FIN dataset is much higher than the noise of the *2D-3D-S* dataset, we reduce this threshold to 70%. The used parameters for the FIN experiment are summarized in the second row of Table 5.4.

5.2 Results

This section deals with the results of the experiments. The individual results of both experiments are presented and analyzed. Lastly, the results are compared.

5.2.1 2D-3D-S

We ran RSPD, OPS, 3D-KHT, and OBRG on 139 scenes of the *2D-3D-S* dataset. Subsequently, for each scene, the *Precision, Recall,* and the *F1-Score* of each algorithm were calculated. The computation times were measured and divided into pre-processing t_{pre}, plane detection t_{calc}, and post-processing t_{post}. Table 5.5 shows the average of the computed results for each algorithm. The rightmost column gives the total computation time t_{tot}. The largest values of the accuracy and the smallest average values of the times are indicated in bold. It is to be noted that no lowest value of t_{post} is indicated since RSPD and 3D-KHT have no post-processing steps and, therefore, "per default" spend less time in this step.

Algorithm	Precision	Recall	F1-Score	t_{pre}	t_{calc}	t_{post}	t_{tot}
RSPD	84.80%	**89.79%**	**86.84%**	62.65	1.04	/	63.69
OPS	**88.98%**	70.45%	77.68%	13.12	10.97	1.01	25.10
3DKHT	71.40%	78.32%	75.19%	**0.71**	**1.03**	/	**1.74**
OBRG	81.38%	66.77%	71.00%	28.07	34.29	2.61	62.97

Table 5.5: Average results of each algorithm over the *2D-3D-S* dataset. The right half of the inner columns shows the average time spent in pre-processing (t_{pre}), the average time spent in the plane detection (t_{calc}), and the average time spent in post-processing steps (t_{post}). The rightmost column shows the average total calculation time t_{tot}. Note, that the absence of post-processing steps is denoted as "/". All times are measured in seconds.

Accuracy RSPD has the overall highest accuracy with a *Precision* of ∼85%, a *Recall* of ∼90%, and an *F1-Score* of ∼87%. OPS supersedes RSPD with a *Precision* value of ∼89% but scores significantly lower *Recall* and *F1-Score* values. 3D-KHT yields *Precision*, *Recall* and *F1-Score* results in the range of ∼71% and ∼79%. OBRG has a high *Precision* value of ∼81%, however its *Recall* and *F1-Score* values are the lowest out of all algorithms with ∼67% and ∼71%, respectively.

Average Time With an average of $0.71s$ spent in pre-processing, and an average of $1.03s$ spent in plane detection, 3D-KHT only needs an average total of $1.74s$ to process an entire point cloud and thereby achieves the lowest calculation times. RSPD is the only algorithm that scores similar t_{calc} values, with an average of $1.04s$. However, RSPD's time spent in pre-processing is the highest among the algorithms. With an average t_{tot} of $\sim 25s$ and $\sim 63s$, OPS and OBRG, respectively, run dramatically slower than the other two algorithms. According to these values, no algorithm achieves *total real-time* applicability. RSPD and 3D-KHT are very close to falling under the threshold of $1s$ for *real-time plane detection*, exceeding it by only $0.4s$ and $0.3s$, respectively

Relationship of Time and Size For each scene of the *2D-3D-S* dataset, the pairs of processing times and point cloud file sizes are presented in Figure 5.1.

The computation times of 3D-KHT do not seem to strongly relate to the size of the point cloud. Both the duration of the pre-processing and the duration of the plane detection initially grow linearly but do not show a large growth even with large jumps in point cloud size. The difference in calculation times between $\sim 280mb$ and $>400mb$ is hardly noticeable.

The computation times of RPSD show a similar relation, with the difference that the pre-processing of RSPD takes significantly longer. As with 3D-KHT, the duration of plane detection seems to have an upper limit.

In general, the pre-processing time of OPS has a linear growth depending on the size of the point cloud. The duration of plane detection also shows a linear relationship, with the difference that there is a certain level of fluctuation. The post-processing times are negligible for the most part, given the small number of values above 0. The irregularity of the spikes gives reason to assume that it primarily depends on the structure of the recorded environment rather than size alone.

The duration of the pre-processing of OBRG also shows a linear relationship with respect to the point cloud size. The average high t_{pre} values from Table 5.5 are also reflected here since most values are in the range of $10s - 100s$, even for smaller cloud sizes at $\sim 25mb$. The t_{calc} values of OBRG do not appear to be dependent on the size of the point cloud, as the computation times tend to decrease with growing point clouds. A possible reason could be the fixed value of the octree levels l_{max}. As this parameter is vital for the calculations in all phases, all calculation times of OBRG are likely to show improvement upon applying a parameter optimization of l_{max} based on the dataset. From our experience, the mid-sized scenes in the *2D-3D-S* dataset are often long and narrow hallways. Assuming an inappropriate octree depth parameter, the subdivision could effectively split the hallway, returning a set of chunks that are in no way to be considered planar. This would consequently lead to an early termination due to failed thresholds, thus reducing the calculation times (and most likely yielding low accuracy).

Summary 2D-3D-S Experiment With an average of $\sim 89\%$, OPS has the highest value in *Precision*, while RSPD achieves the highest *Recall* and *F1-Score* with $\sim 90\%$ and $\sim 87\%$, respectively. 3D-KHT has the lowest total computation time t_{tot} with an average of $1.74s$. With $>60s$, RSPD and OBRG have the largest t_{tot} values among the algorithms, with t_{pre} accounting for the majority for RSPD.

Figure 5.1 shows that the runtimes of 3D-KHT are the smallest. RSPD also has low t_{calc} values but consistently spends the longest time in pre-processing. Moreover, the

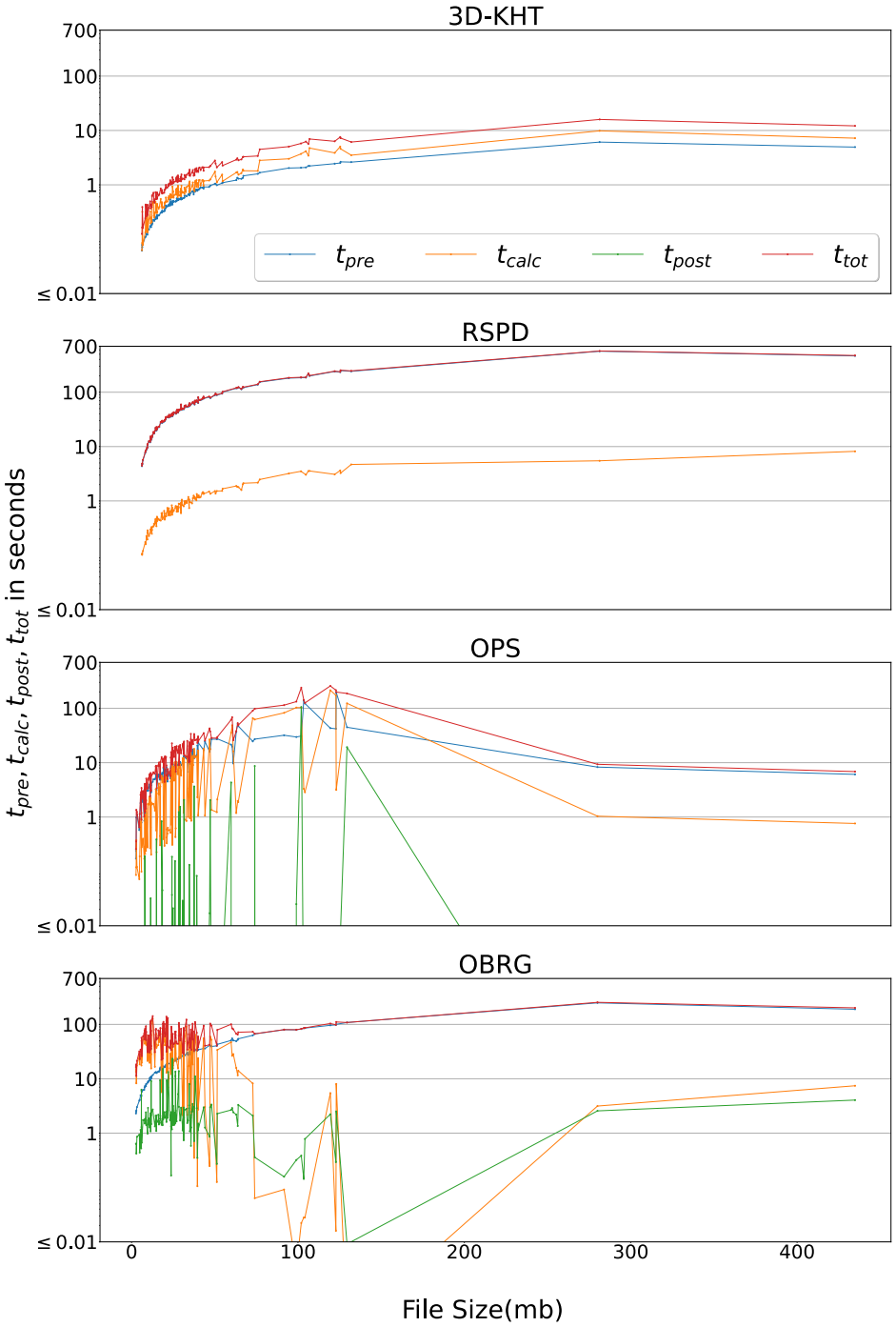

Figure 5.1: The time spent in pre-processing t_{pre}, plane detection t_{calc}, post-processing t_{post}, and the total calculation time t_{tot} per point cloud file size of the *2D-3D-S* dataset. Note, that the y-axis is scaled logarithmically to the base of ten.

pre-processing times of all algorithms seem to be generally dependent on the size of the point cloud. The plane detection runtimes of OPS and OBRG fluctuate. However, OPS fluctuates less than OBRG. The post-processing runtimes of OPS are negligible overall. The t_{post} values of OBRG are stable at $2.61s$ on average, except for medium cloud sizes, see table 5.5.

Adhering strictly to our definitions of real-time, no algorithm achieves real-time applicability in this experiment. However, we might consider RSPD and 3D-KHT to be *real-time plane detection* applicable since the point cloud sizes vary greatly, and the average duration of their plane detection phase is only $0.03s-0.04s$ greater than the $1s$ threshold. Furthermore, as Figure 5.1 suggests, RSPD and 3D-KHT are *real-time plane detection* applicable for point clouds with a size $\lesssim 40mb$, or $\lesssim 1.5 \cdot 10^6$ points.

5.2.2 FIN

Each of the total 708 time frames of the FIN data set was processed by each algorithm. Subsequently, we evaluated each time frame separately, i.e., by calculating the *Precision, the Recall,* and the *F1-Score* . Additionally, we measured the computation times of each time frame for all algorithms, again divided into pre-processing t_{pre}, plane detection t_{calc}, and post-processing t_{post}.

The average results over all time steps of all scenes of the FIN experiment are presented in Table 5.6. The highest values are written in bold for *Precision, Recall,* and the *F1-Score*, as are the lowest times of each calculation step and the total time.

Algorithm	Precision	Recall	F1-Score	t_{pre}	t_{calc}	t_{post}	t_{tot}
RSPD	57.30%	**60.75%**	**58.70%**	14.36	**0.19**	/	14.55
OPS	**69.38%**	29.23%	39.43%	4.61	0.89	0.13	5.63
3DKHT	49.76%	44.40%	46.48%	**0.14**	0.29	/	**0.43**
OBRG	49.23%	27.42%	33.94%	6.03	14.70	0.35	21.08

Table 5.6: Average Results of the FIN experiment. Shown are the average values of all scenes and time frames, sorted by algorithm. The right half of the columns shows the average time spent in pre-processing (t_{pre}), the average time spent in the plane detection itself (t_{calc}), and the average time spent in post-processing steps (t_{post}). The rightmost column shows the average total calculation time s_{tot}. Note, that the absence of post-processing steps is denoted as "/". All times are measured in seconds.

Accuracy OPS has the highest average *Precision* of the algorithms, with almost 70%. RSPD achieves the highest values for *Recall* and the *F1-Score* with ∼61% and ∼59%, respectively. 3D-KHT and OBRG achieve a similar *Precision*, but for *Recall* and *F1-Score*, however, 3D-KHT has higher values than OBRG by approx. 13% and approx. 17%, respectively. RSPD thus achieves the highest overall accuracy, while OBRG achieves the overall lowest.

Average Time With almost $15s$, RSPD spends the most time in pre-processing among the algorithms. In contrast, RSPD has the shortest time spent during plane detection, with an average of $0.19s$. Overall, 3D-KHT needs the shortest time for the complete computation t_{tot} of a time step with an average of $0.43s$. OPS achieves comparatively average total calculation time with $\sim 6s$, and OBRG takes the longest overall to compute a time step with more than $20s$.

RSPD and 3D-KHT achieve *real-time plane detection* applicability. Additionally, 3D-KHT also achieves *total real-time* applicability, with an average total time of $0.43s$. OPS can almost be considered to be in RT_{calc} with a subtotal calculation time of $1.02s$, thereby taking $0.02s$ too long. With an average pre-processing time of $\sim 6s$ and an average of $\sim 15s$ spent in plane detection, OBRG qualifies for neither of the introduced definitions of *real-time*.

Relationship of Time and Size As mentioned before, we consider the relationship between the size of the point cloud and the corresponding calculation time. In Figure 5.2, we compare the processing times of each time step to the file size of the *auditorium* scene of the FIN data set.

Note, that we created similar graphs for the other scenes of the FIN dataset. However, they do not introduce new information into the argumentation and are presented in the appendix **$REF** for completeness and spatial reasons. The auditorium scene was selected as the most representative because it contains the longest recording, and thus contains the most data.

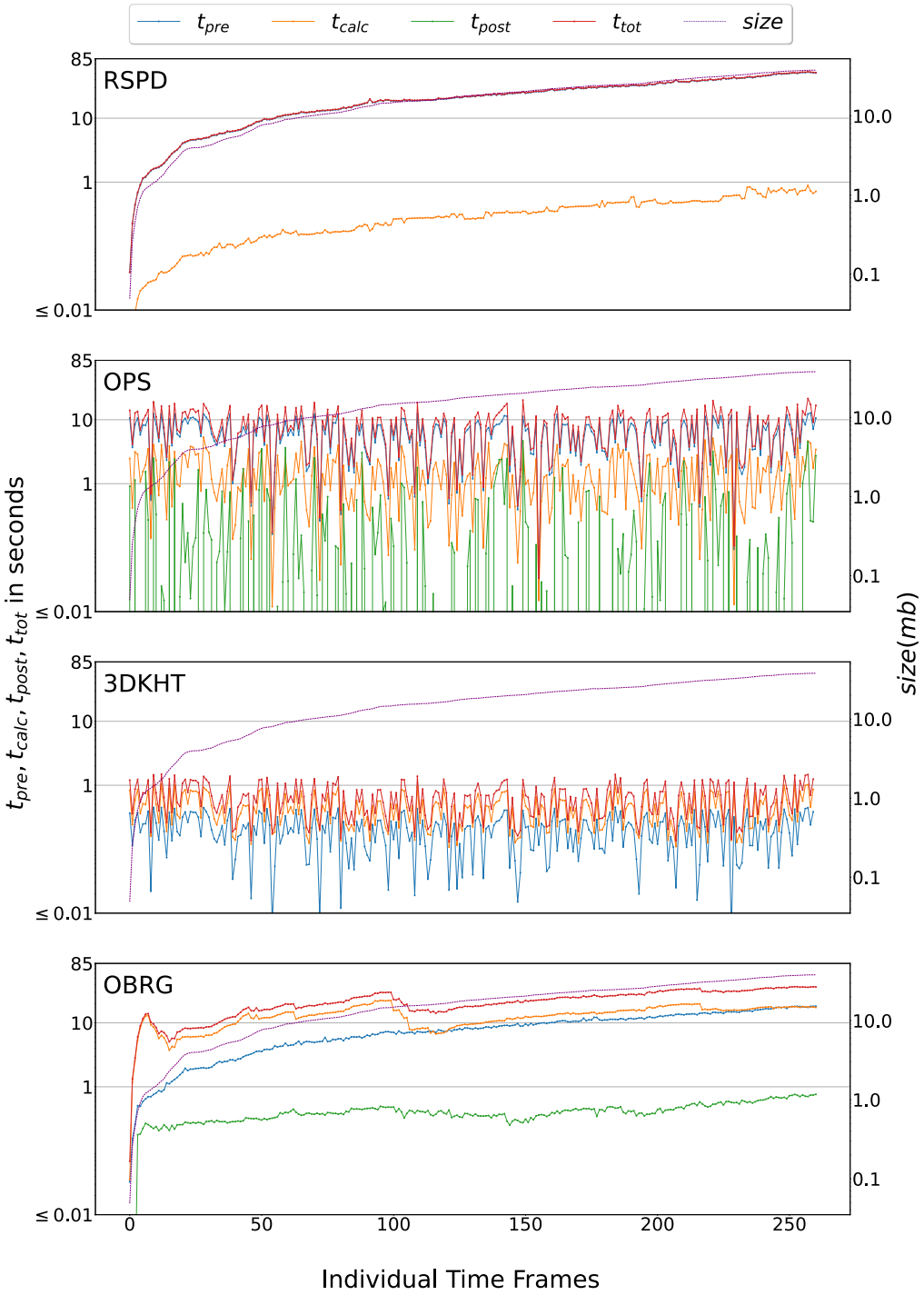

Figure 5.2: Time spent in pre-processing t_{pre}, plane detection t_{calc}, post-processing t_{post}, and total calculation time t_{tot} of the auditorium scene and cloud sizes $size$ of each time frame. Note, that both y-axes are scaled logarithmically to the base of ten. *Time Frames* are defined in Subsection 5.1.1.

The pre-processing times of RSPD and OBRG are noticeably proportional to the point cloud size. In contrast, for OPS and 3D-KHT, the pre-processing times seem to correlate with the plane detection times since both show similar spikes. The plane detection steps of OPS and 3D-KHT do not seem to depend on the point cloud size, as both seem to be limited by an upper bound ($\sim 1s$ for 3D-KHT and $\sim 6s$ for OPS). The pre-processing and plane detection times of OBRG grow rapidly in the beginning but afterward, show a linear growth in relation to the cloud size. The post-processing times of OPS fluctuate between 0 and the duration of plane detection. After the spike in the beginning, the t_{post} values of OBRG seem to be consistent.

The apparent upper bound of $\sim 1s$ in the calculation times qualifies 3D-KHT for *total real-time* applicability. We consider RSPD *real-time plane detection* applicable, as the duration of the plane detection step consistently stays under $1s$.

Summary FIN Experiment OPS has the highest average *Precision*, and RSPD has the largest percentages of *Recall* and the *F1-Score* . Additionally, RSPD has the lowest t_{calc} value among the algorithms, with an average of $0.19s$ per time frame. In contrast, RSPD has the longest pre-processing time with $14.36s$ on average. The algorithm with the shortest pre-processing and the shortest total time is 3D-KHT with $t_{pre} = 0.14s$ and $t_{tot} = 0.43s$, respectively.

In general, the calculation times of RSPD and OBRG seem to depend on the point cloud size. However, the time RPSD spends in pre-processing is significantly higher than in its plane detection step. In contrast, the pre-processing and plane detection times of OBRG seem to converge at the end. The calculation times of OPS and 3D-KHT seem to be independent of the point cloud size and consistently stay under an upper bound. However, 3D-KHT has a smaller upper bound than OPS.

The development over time supports the average calculation times of 3D-KHT, as the calculation seems independent of the cloud size. Thereby, we determine 3D-KHT to be *total real-time* applicable. Furthermore, RSPD achieves *real-time plane detection* in the FIN experiment, as the plane detection step takes $< 1s$ for all time frames. Lastly, the average subtotal calculation time of OPS is slightly longer than $1s$. However, given the apparent upper bound and considerable fluctuations, we cautiously consider OPS to be *real-time plane detection* applicable in the FIN experiment.

5.2.3 Comparison

When comparing Table 5.5 and Table 5.6, a pattern emerges: OPS has the highest *Precision* value, RSPD yields the highest *Recall* and *F1-Score*, and 3D-KHT has the lowest average total processing time.

Observing Figure 5.2 and Figure 5.1, common features are noticeable: The curve shape of RSPD is very similar for both experiments, linearly dependent on the point cloud size, and the t_{pre} accounts for 99% of the total calculation time t_{tot}. In both experiments, the post-processing time of OPS fluctuates. The post-processing of OBRG seems to be oriented around a given value, however, this value differs between the experiments ($\sim 0.3s$ for the FIN experiment and $\sim 3s$ for the *2D-3D-S* experiment). 3D-KHT scores very low processing times in both experiments.

However, there are also notable differences. Whereas the calculation times of 3D-KHT seem to be proportional to the point cloud size in the *2D-3D-S* experiment, they show no such relation during the FIN experiment. It is, however, noteworthy that the cloud sizes widely differ between the experiments, as the maximum size of the FIN experiment ($\sim 30mb$) is very small, compared to largest scene of the *2D-3D-S* dataset ($>400mb$). Nonetheless, since Figure 5.1 portrays a proportionality, even for smaller clouds, the reason for different curves is likely the difference of parameterization.

In Paragraph 5.2.1, we report that no algorithm is *real-time* applicable. We state, that RSPD and 3D-KHT can be considered *real-time plane detection* applicable, since the cloud sizes vary and the difference between their average t_{calc} times and the threshold of $1s$ is very small. In Paragraph 5.2.2, we consider 3D-KHT *totally real-time* applicable due to the observed upper bound in calculation time in combination with a low average t_{tot} value of $0.43s$. Additionally, we consider $RSPD \in RT_{calc}$ because RSPD takes consistently less than $1s$ during the plane detection step. The results of neither experiment show a *real-time* applicability of OBRG.

5.3 Summary

OBRG does not achieve the highest or lowest values in any experiment. OPS has the highest *Precision* in both experiments. Due to *Recall* and the *F1-Score*, RSPD has the highest overall accuracy in both experiments. The pre-processing of RSPD takes the longest time of all algorithms. In contrast, RSPD has the smallest average t_{calc} value in the FIN experiment. 3D-KHT has the lowest total computation time in both experiments, and in the *2D-3D-S* experiment, it outperforms the plane detection time of RSPD.

3D-KHT is *real-time plane detection* applicable in both experiments, *totally real-time* applicable in the FIN experiment, even. RSPD achieves *real-time plane detection* in both experiments. We consider OPS to be *real-time plane detection* applicable. These *real-time* applicabilities of all algorithms are summarized in Table 5.7.

Experiment	RSPD	OPS	3D-KHT	OBRG
2D-3D-S	RT_{calc}*	/	RT_{calc}*	/
FIN	RT_{calc}	RT_{calc}*	RT_{tot}	/

Table 5.7: Real-time applicabilities of the selected plane detection algorithms given the results from both experiments. Note, that RT_{tot} implies RT_{calc}. "/" denotes no real-time applicability. "*" denotes that the given real-time applicability is coupled with a restriction. We refer to the text for details.

6 Conclusion and Future Work

6.0.1 Summary

Use case, scenario, real-world application, current problem Viele AR/VR anwendungen benutzen plane detection.. Echtzeit ist wichtig.. Es werden spezielle Sensoren benötigt, ein SLAM algo und ein geeigneter plane detection algo.. Die Auswahl des besten plane detection algorithmus ist nicht trivial..

Daher das thema dieser arbeit Wir vergleichen algorithmen mit fokus auf die echtzeitfähigkeit wir haben 2 definitionen für echtzeit angegeben.. Wir beschränken uns in dieser arbeit auf plane detection mit intel realsense technologie das beinhaltet 2 kameras und die dazugehörige software (+SLAM)

algorithmen Es wurde die aktuelle literatur gelesen und eine liste aus algorithmen erstellt. Es wurden metriken zum objektiven und oberflächlichen Vergleich der algorithmen angegeben basierend auf den metriken wurden vier algorithmen für einen vergleich ausgewählt

Testscenario / datensatz Da die ausgewählten algorithmen nicht auf dem selben Datensatz getestet wurden haben wir geeignete ausgesucht. Wir haben uns für den *2D-3D-S* Datensatz entschieden.. motiviert durch die abwesenheit eines datensatzes mit temporaler komponente haben wir einen eigenen datensatz erstellt

Experimentaufbau Da wir zwei datensätze haben haben wir auch zwei experimente Zunächst wurden bewertungsmetriken der datensätze eingeführt: precision, recall, f1, dazu wurden die berechnungszeiten genau gemessen und es wird unterschieden in preprocessing, plane detection und post-processing. diese experimente wurden seperat durchgeführt und ausgewertet im anschluss darauf wurden die ergebnisse beider Experimente verglichen

Ergebnisse der Experimente die ergebnisse lassen sich zusammenfassen in: 3D-KHT ist der insgesamt schnellste RSPD ist der insgesamt präziseste

wir haben zwei definitionen von echtzeit gemäß dieser definitionen und anhand der ergebnisse aus dem letzten kapitel gilt: (in einem realwelt environment)

- 3D-KHT $\in RT_{tot}$, da $t_{tot} < 1$
- RSPD $\in RT_{calc}$, da $t_{calc} < 1$

6.0.2 Fazit

OBRG ist nicht echtzeitfähig.

Da das pre-processing von RSPD viel zu lange dauert ist RSPD insgesamt nicht total echtzeitfähig, die echtzeitfähigkeit beschränkt sich somit auf die plane detection phase.

OPS erzielt im FIN experiment so grade werte die für eine plane detection echtzeit sprechen würden. Auch hier dauert das pre-processing zu lange um von einer totalen echtzeit sprechen zu können.

3D-KHT ist im FIN experiment deutlich unter der Schranke von einer sekunde, damit in einem realen enviroment total echtzeitfähig.

Limitationen der ergebnisse Ein Faktor der langsamen laufzeit von OBRG ist definitiv die implementation. Python ist aus diversen Gründen magnituden langsamer als C++ und es wurde bei der anfertigung der implementation die präzision priorosiert da durch die wahl der programmiersprache sowieso nicht von echtzeitfähigkeit ausgegangen wurde.

3D-KHT ist der schnellste algorithmus, lässt aber leider in sachen accuracy viele prozente liegen.

Algo x ist der beste, mögl verbesserungen Das einzige was RPSD von einer eindeutigen dominanz trennt ist die Dauer des preprocessings. In RPSD's pre-processing phase werden die normalen der Punktwolke berechnet. Es ist möglich dass die normalen noch vor der plane detection phase aus Figure 3.1 berechnet werden. Zb kann sogar die intel realsense technologie die normalen exportieren. Dies würde nach angemessenen anpassungen des algorithmuses die Berechnungszeiten auf t_{calc} reduzieren. Somit würde RSPD ebenfalls total echtzeitfähig sein.

Diese anpassung des experiments würde einen bias gegenüber RSPD darstellen, weswegen wir das unterlassen haben und als weitere aufgabe nach dem abschluss dieser arbeit ansehen.

Ebenso interessant sind die Laufzeiten einer optimierten implementierung von OBRG in C++.

Die parametrisierung von 3D-KHT ist definitiv die komplizierteste aus den algorithmen und hat daher das größte optimierungspotential. Das ist in dem fall ein doppelschneidiges schwert, da zuerst eine optimale/ausreichende parametrisierung gefunden werden muss, bevor der algorithmus das volle potential entfaltet.

Bibliography

[1] Abner M. C. Araújo and Manuel M. Oliveira. "A robust statistics approach for plane detection in unorganized point clouds". In: *Pattern Recognition* 100 (2020), pp. 107–115.

[2] I. Armeni, A. Sax, A. R. Zamir, and S. Savarese. "Joint 2D-3D-Semantic Data for Indoor Scene Understanding". In: *ArXiv e-prints* (2017). arXiv: 1702.01105 [cs.CV].

[3] Ramy Ashraf and Nawal Ahmed. "FRANSAC: Fast RANdom Sample Consensus for 3D Plane Segmentation". In: *International Journal of Computer Applications* 167.13 (2017), pp. 30–36.

[4] Michael Bloesch, Michael Burri, Sammy Omari, Marco Hutter, and Roland Siegwart. "Iterated extended Kalman filter based visual-inertial odometry using direct photometric feedback". In: *The International Journal of Robotics Research* 36.10 (2017), pp. 1053–1072.

[5] Dorit Borrmann, Jan Elseberg, Kai Lingemann, and Andreas Nüchter. "The 3D Hough Transform for plane detection in point clouds: A review and a new accumulator design". In: *3D Research* 2.2 (2011), p. 3.

[6] Carlos Campos, Richard Elvira, Juan J Gómez Rodriguez, José MM Montiel, and Juan D Tardós. "Orb-slam3: An accurate open-source library for visual, visual–inertial, and multimap slam". In: *IEEE Transactions on Robotics* 37.6 (2021), pp. 1874–1890.

[7] Aparicio Carranza, Juan Estrella, Rashid Zaidi, and Harrison Carranza. "Plane Detection Based Object Recognition for Augmented Reality". In: May 2021. DOI: 10.11159/cdsr21.305.

[8] Andrew J Davison, Ian D Reid, Nicholas D Molton, and Olivier Stasse. "MonoSLAM: Real-time single camera SLAM". In: *IEEE transactions on pattern analysis and machine intelligence* 29.6 (2007), pp. 1052–1067.

[9] Richard O. Duda and Peter E. Hart. "Use of the Hough Transformation to Detect Lines and Curves in Pictures". In: *Commun. ACM* 15.1 (1972), pp. 11–15.

[10] Felix Endres, Jürgen Hess, Jürgen Sturm, Daniel Cremers, and Wolfram Burgard. "3-D mapping with an RGB-D camera". In: *IEEE transactions on robotics* 30.1 (2013), pp. 177–187.

[11] Jakob Engel, Vladlen Koltun, and Daniel Cremers. “Direct sparse odometry”. In: *IEEE transactions on pattern analysis and machine intelligence* 40.3 (2017), pp. 611–625.

[12] Chen Feng, Yuichi Taguchi, and Vineet R. Kamat. “Fast plane extraction in organized point clouds using agglomerative hierarchical clustering”. In: *IEEE International Conference on Robotics and Automation*. IEEE, 2014, pp. 6218–6225.

[13] A. Handa, T. Whelan, J.B. McDonald, and A.J. Davison. “A Benchmark for RGB-D Visual Odometry, 3D Reconstruction and SLAM”. In: *IEEE Intl. Conf. on Robotics and Automation, ICRA*. 2014.

[14] Ankur Handa, Thomas Whelan, John McDonald, and Andrew J. Davison. “A benchmark for RGB-D visual odometry, 3D reconstruction and SLAM”. In: *IEEE International Conference on Robotics and Automation*. IEEE, 2014, pp. 1524–1531.

[15] Peter E. Hart. “How the Hough transform was invented [DSP History]”. In: *IEEE Signal Processing Magazine* 26.6 (2009), pp. 18–22.

[16] Kaiming He, Georgia Gkioxari, Piotr Dollár, and Ross Girshick. “Mask r-cnn”. In: *Proceedings of the IEEE international conference on computer vision*. 2017, pp. 2961–2969.

[17] Kaiming He, Xiangyu Zhang, Shaoqing Ren, and Jian Sun. “Deep Residual Learning for Image Recognition”. In: arXiv:1512.03385 (2015). arXiv:1512.03385 [cs].

[18] Alejandro Hidalgo-Paniagua, Miguel A. Vega-Rodriguez, Nieves Pavón, and Joaquin Ferruz. “A Comparative Study of Parallel RANSAC Implementations in 3D Space”. In: *International Journal of Parallel Programming* 43.5 (2015), pp. 703–720.

[19] Adam Hoover, Gillian Jean-Baptiste, Patrick Flynn, Horst Bunke, Dmitry Goldgof, Kevin Bowyer, David Eggert, Andrew Fitzgibbon, and Robert Fisher. “An Experimental Comparison of Range Image Segmentation Algorithms”. In: *IEEE Trans. Pattern Anal. Mach. Intell.* 18 (1996), pp. 673–689.

[20] Daniel Huber. “The ASTM E57 File Format for 3D Imaging Data Exchange”. In: *Proceedings of SPIE Electronics Imaging Science and Technology Conference, 3D Imaging Metrology*. Vol. 7864. 2011.

[21] Lam Huynh, Phong Nguyen-Ha, Jiri Matas, Esa Rahtu, and Janne Heikkila. “Guiding Monocular Depth Estimation Using Depth-Attention Volume”. In: arXiv:2004.02760 (2020). arXiv:2004.02760 [cs].

[22] Christian Kerl, Jurgen Sturm, and Daniel Cremers. “Dense visual SLAM for RGB-D cameras”. In: *IEEE/RSJ International Conference on Intelligent Robots and Systems*. IEEE, 2013, pp. 2100–2106.

[23] Davis E. King. “Dlib-ml: A Machine Learning Toolkit”. In: *Journal of Machine Learning Research* 10 (2009), pp. 1755–1758.

[24] Mathieu Labbé and François Michaud. “RTAB-Map as an open-source lidar and visual simultaneous localization and mapping library for large-scale and long-term online operation: LABBÉ and MICHAUD”. In: *Journal of Field Robotics* 36.2 (2019), pp. 416–446.

[25] Frederico A. Limberger and Manuel M. Oliveira. “Real-Time Detection of Planar Regions in Unorganized Point Clouds”. In: *Pattern Recognition* 48.6 (2015), pp. 2043–2053.

[26] Tsung-Yi Lin, Piotr Dollár, Ross Girshick, Kaiming He, Bharath Hariharan, and Serge Belongie. “Feature Pyramid Networks for Object Detection”. In: arXiv:1612.03144 (2017). arXiv:1612.03144 [cs].

[27] Chen Liu, Kihwan Kim, Jinwei Gu, Yasutaka Furukawa, and Jan Kautz. “PlaneRCNN: 3D Plane Detection and Reconstruction From a Single Image”. In: *IEEE/ Conference on Computer Vision and Pattern Recognition*. IEEE, 2019, pp. 4445–4454.

[28] Chen Liu, Jimei Yang, Duygu Ceylan, Ersin Yumer, and Yasutaka Furukawa. “PlaneNet: Piece-Wise Planar Reconstruction from a Single RGB Image”. In: *IEEE/ Conference on Computer Vision and Pattern Recognition*. IEEE, 2018, pp. 2579–2588.

[29] Andréa Macario Barros, Yoann Moline, Frédérick Carrel, Maugan Michel, and Gwenolé Corre. “A Comprehensive Survey of Visual SLAM Algorithms”. In: *Robotics* 11 (2022).

[30] Aminah Abdul Malek, Wan Eny Zarina Wan Abdul Rahman, Siti Salmah Yasiran, Abdul Kadir Jumaat, and Ummu Mardhiah Abdul Jalil. “Seed point selection for seed-based region growing in segmenting microcalcifications”. In: *International Conference on Statistics in Science, Business and Engineering (ICSSBE)*. IEEE, 2012, pp. 1–5.

[31] Hannes Mols, Kailai Li, and Uwe D. Hanebeck. “Highly Parallelizable Plane Extraction for Organized Point Clouds Using Spherical Convex Hulls”. In: *IEEE International Conference on Robotics and Automation*. IEEE, 2020, pp. 7920–7926.

[32] Raúl Mur-Artal and Juan D. Tardós. “ORB-SLAM2: An Open-Source SLAM System for Monocular, Stereo, and RGB-D Cameras”. In: *IEEE Transactions on Robotics* 33.5 (Oct. 2017), p. 12551262. ISSN: 1941-0468. DOI: 10.1109/TRO.2017.2705103.

[33] V. Nguyen, A. Martinelli, N. Tomatis, and R. Siegwart. “A comparison of line extraction algorithms using 2D laser rangefinder for indoor mobile robotics”. In: *IEEE/RSJ International Conference on Intelligent Robots and Systems*. 2005, pp. 1929–1934.

[34] Bastian Oehler, Joerg Stueckler, Jochen Welle, Dirk Schulz, and Sven Behnke. "Efficient Multi-resolution Plane Segmentation of 3D Point Clouds". In: *Intelligent Robotics and Applications*. Vol. 7102. Springer Berlin Heidelberg, 2011, pp. 145–156.

[35] Pedro F. Proenca and Yang Gao. "Probabilistic RGB-D Odometry based on Points, Lines and Planes Under Depth Uncertainty". In: arXiv:1706.04034 (2018). arXiv:1706.04034 [cs].

[36] Pedro F. Proença and Yang Gao. "Fast Cylinder and Plane Extraction from Depth Cameras for Visual Odometry". In: arXiv:1803.02380 (2018). number: arXiv:1803.02380 arXiv:1803.02380 [cs].

[37] Olaf Ronneberger, Philipp Fischer, and Thomas Brox. "U-net: Convolutional networks for biomedical image segmentation". In: *International Conference on Medical image computing and computer-assisted intervention*. Springer. 2015, pp. 234–241.

[38] Arindam Roychoudhury, Marceli Missura, and Maren Bennewitz. "Plane Segmentation Using Depth-Dependent Flood Fill". In: *IEEE/RSJ International Conference on Intelligent Robots and Systems*. IEEE, 2021, pp. 2210–2216.

[39] Arindam Roychoudhury, Marcell Missura, and Maren Bennewitz. "Plane Segmentation in Organized Point Clouds using Flood Fill". In: *IEEE International Conference on Robotics and Automation*. IEEE, 2021, pp. 13532–13538.

[40] Arindam Roychoudhury, Marcell Missura, and Maren Bennewitz. "Plane Segmentation in Organized Point Clouds using Flood Fill". In: *IEEE International Conference on Robotics and Automation*. IEEE, 2021, pp. 13532–13538.

[41] Radu Bogdan Rusu and Steve Cousins. "3D is here: Point Cloud Library (PCL)". In: *IEEE International Conference on Robotics and Automation*. 2011.

[42] Alexander Schaefer, Johan Vertens, Daniel Büscher, and Wolfram Burgard. "A Maximum Likelihood Approach to Extract Finite Planes from 3-D Laser Scans". In: *IEEE/RSJ International Conference on Robotics and Automation*. IEEE. 2019.

[43] Nathan Silberman, Derek Hoiem, Pushmeet Kohli, and Rob Fergus. "Indoor Segmentation and Support Inference from RGBD Images". In: *Computer Vision – ECCV 2012*. Ed. by Andrew Fitzgibbon, Svetlana Lazebnik, Pietro Perona, Yoichi Sato, and Cordelia Schmid. Springer Berlin Heidelberg, 2012, pp. 746–760.

[44] Shuran Song, Samuel P. Lichtenberg, and Jianxiong Xiao. "SUN RGB-D: A RGB-D scene understanding benchmark suite". In: *IEEE Conference on Computer Vision and Pattern Recognition*. 2015, pp. 567–576.

[45] J. Sturm, N. Engelhard, F. Endres, W. Burgard, and D. Cremers. "A Benchmark for the Evaluation of RGB-D SLAM Systems". In: *Proc. of the International Conference on Intelligent Robot Systems*. 2012.

[46] Bo Sun and Philippos Mordohai. “Oriented Point Sampling for Plane Detection in Unorganized Point Clouds”. In: arXiv:1905.02553 (2019). arXiv:1905.02553 [cs].

[47] Eduardo Vera, Djalma Lucio, Leandro A.F. Fernandes, and Luiz Velho. “Hough Transform for real-time plane detection in depth images”. In: *Pattern Recognition Letters* 103 (2018), pp. 8–15.

[48] Anh-Vu Vo, Linh Truong-Hong, Debra F. Laefer, and Michela Bertolotto. “Octree-based region growing for point cloud segmentation”. In: *ISPRS Journal of Photogrammetry and Remote Sensing* 104 (2015), pp. 88–100.

[49] Xinlong Wang, Rufeng Zhang, Tao Kong, Lei Li, and Chunhua Shen. “Solov2: Dynamic and fast instance segmentation”. In: *Advances in Neural information processing systems* 33 (2020), pp. 17721–17732.

[50] Yaxu Xie, Fangwen Shu, Jason Rambach, Alain Pagani, and Didier Stricker. “PlaneRecNet: Multi-Task Learning with Cross-Task Consistency for Piece-Wise Plane Detection and Reconstruction from a Single RGB Image”. In: arXiv:2110.11219 (2022). number: arXiv:2110.11219 arXiv:2110.11219 [cs].

[51] Michael Ying Yang and Wolfgang Forstner. “Plane Detection in Point Cloud Data”. In: *Proceedings of the 2nd int conf on machine control guidance* 1 (2010), p. 16.

[52] Fisher Yu, Vladlen Koltun, and Thomas Funkhouser. “Dilated residual networks”. In: *Proceedings of the IEEE conference on computer vision and pattern recognition*. 2017, pp. 472–480.

[53] Qian-Yi Zhou, Jaesik Park, and Vladlen Koltun. “Open3D: A Modern Library for 3D Data Processing”. In: *arXiv:1801.09847* (2018).

Declaration of Academic Integrity

I hereby declare that I have written the present work myself and did not use any sources or tools other than the ones indicated.

Datum: .....

(Signature)